

H α imaging observations of early-type galaxies from the ATLAS^{3D} survey [★]

G. Gavazzi¹, G. Consolandi¹, S. Pedraglio¹, M. Fossati^{2,3}, M. Fumagalli⁴, and A. Boselli⁵

¹ Università degli Studi di Milano-Bicocca, Piazza della Scienza 3, 20126 Milano, Italy
e-mail: giuseppe.gavazzi@mib.infn.it

² Max-Planck-Institut für Extraterrestrische Physik, Giessenbachstrasse, D-85748 Garching, Germany
e-mail: mfossati@mpe.mpg.de

³ Universitäts-Sternwarte München, Schenierstrasse 1, D-81679 München, Germany.

⁴ Institute for Computational Cosmology, and Centre for Extragalactic Astronomy, Durham University, South Road, Durham, DH1 3LE, UK
e-mail: michele.fumagalli@durham.ac.uk

⁵ Aix Marseille Université, CNRS, LAM (Laboratoire d'Astrophysique de Marseille) UMR 7326, F-13388, Marseille, France
e-mail: alessandro.boselli@lam.fr

Received; accepted

ABSTRACT

Context. The traditional knowledge of the mechanisms that caused the formation and evolution of early-type galaxies (ETG) in a hierarchical universe was challenged by the unexpected finding by ATLAS^{3D} that 86% of the ETGs show signs of a fast-rotating disk at their interior. This implies a common origin of most spiral galaxies, followed by a quenching phase, while only a minority of the most massive systems are slow rotators and were likely to be the products of merger events.

Aims. Our aim is to improve our knowledge on the content and distribution of ionized hydrogen and their usage to form stars in a representative sample of ETGs for which the kinematics and detailed morphological classification were known from ATLAS^{3D}.

Methods. Using narrow-band filters centered on the redshifted H α line along with a broad-band (*r*-Gunn) filter to recover the stellar continuum, we observed or collected existing imaging observations for 147 ETGs (including members of the Virgo cluster) that are representative of the whole ATLAS^{3D} survey.

Results. Fifty-five ETGs (37%) were detected in the H α line above our detection threshold, ($H\alpha E.W. \leq -1\text{\AA}$), and 21 harbor a strong source ($H\alpha E.W. \leq -5\text{\AA}$).

Conclusions. The strong H α emitters appear associated with mostly low-mass ($M_* \sim 10^{10} M_\odot$) S0 galaxies that contain conspicuous stellar and gaseous discs. These harbor significant star formation at their interior, including their nuclei. The weak H α emitters are almost one order of magnitude more massive, contain gas-poor discs and harbor an AGN at their centers. Their emissivity is dominated by [NII] and does not imply star formation. The 92 undetected ETGs constitute the majority in our sample and are gas-free systems that lack a disc and exhibit passive spectra even in their nuclei. These pieces of evidence reinforce the conclusion made previously that the evolution of ETGs followed the secular channel for the less massive systems and the dry merging channel for the most massive galaxies at the center of clusters of galaxies.

Key words. Galaxies: evolution – Galaxies: Early-type; Galaxies: fundamental parameters – Galaxies: star formation

1. Introduction

Our understanding of the processes that caused the formation of galaxies and their subsequent evolution must cope with the observational evidence that today, galaxies are distributed in a bimodal population (Kauffmann et al. 2003, Balogh et al. 2004, Baldry et al. 2004): the blue cloud, composed of star-forming gas-rich disk systems, and the red sequence made of quiescent gas-poor “red and dead” galaxies. Galaxies are assumed to migrate from the star-forming blue cloud to the red sequence owing to a variety of quenching mechanisms. It is common belief that in a hierarchical universe the main process that brought early-type galaxies (ETGs) across the green valley was merging of disk systems (late-type galaxies; LTGs). These catastrophic events should have dissipated angular momentum of the

pre-merging LTGs, producing non- or slowly rotating elliptical dispersion-dominated galaxies.

However, until the advent of integral field spectrographs, the fraction of true ellipticals (i.e., slow rotators, the outcome of mergers) could only be deduced by the optical morphology of galaxies without any knowledge of the stellar kinematics. Owing to the SAURON IFU spectrograph, the recent ATLAS^{3D} survey (Cappellari et al. 2011) derived resolved stellar kinematic maps of 260 ETGs and for the first time studied the kinematic morphology-density relation using fast and slow rotators instead of ellipticals (E) and lenticulars (S0) (Cappellari et al. 2011b). The survey showed that ETGs are dominated (86%) by fast rotators up to intermediate stellar masses (Emsellem et al. 2011), and from the lowest density environments up to the dense core of the Virgo cluster where only a small increase in the fraction of slow rotators is found. True ellipticals (i.e., slow rotators) are only found among the most massive ETGs and always have an ellipticity lower than 0.4, while lenticulars (i.e., fast ro-

[★] based on observations taken at the Mexican Observatorio Astronómico Nacional and at the Loiano telescope belonging to the Bologna Observatory.

tators) are less massive galaxies and span all possible different ellipticities (Cappellari et al. 2016). This new evidence challenged the paradigm stating that most ETGs are mainly created by merging events, and it opened a revision of the classic tuning-fork scheme that includes the kinematic information. Here, the fast rotators (namely S0s) follow a sequence parallel to spirals. The final outcome of the ATLAS^{3D} survey can be summarized as in Cappellari (2016): Fast-rotator ETGs were originally star-forming disks and evolved owing to secular phenomena, e.g. gas accretion, bulge growth, and quenching. On the opposite slow rotators assembled around massive halos at high redshift via gas poor merging. The dichotomy in stellar mass between the fast rotators and the more massive slow rotators has also been reproduced in recent simulations (Bois et al. 2011; Penoyre et al. 2017) and was reinforced by the findings of even more recent surveys such as the MASSIVE survey (Veale et al. 2017), which demonstrates that only the most massive ETGs ($M_* > 10^{11.5} M_\odot$) are true slow rotators and are perhaps the only genuine outcomes of equal-mass merger events. These ETGs represent the majority of central massive haloes, such as cD galaxies in clusters of galaxies. On the other hand, less massive fast rotators, which represent the vast majority of ETGs, likely emerge from less dramatic evolutionary paths that leave them enough angular momentum to be supported by rotation.

Hence, in addition to mergers (Kauffmann et al. 1993), other secular (e.g., bar instability; Gavazzi et al. 2015) and environmental processes (Boselli & Gavazzi 2006, 2014) need to be invoked to explain the population of the color-luminosity plane. Which processes caused the migration of galaxies across the green valley (perhaps in both directions; Yıldız et al. 2017) is still a matter of debate. This controversy has been tried to be resolved through many lines of research, which were focused on understanding the processes that govern the transformation efficiency of gas (HI and H₂) into stars as a function of stellar mass, morphology, and environment. Ongoing surveys that exploit integral field spectroscopy, such as CALIFA (Sanchez et al. 2012), SAMI (Bryant et al. 2015), and MaNGA (Belfiore et al. 2016), are about to provide us with spatially resolved diagnostic diagrams that will eventually contribute to solving the current controversy.

As the SAURON IFU does not include the $H\alpha$ line in its bandpass, we decided to investigate in this work the ionized hydrogen content of ETGs that were selected by ATLAS^{3D} by means of imaging observations taken through narrow-band (80 Å) filters, combined with a spectroscopic investigation of their nuclear activity. To this end, we combined existing spectroscopy (for the most part from Ho et al, 1995 and from SDSS DR13 Albareti et al. 2016) with observations obtained using the Loiano telescope at the Bologna Observatory. The imaging observations, carried out at the 2.1m telescope at San Pedro Martir (SPM), are described in Section 3, and their calibration is described in Section 4, while our nuclear spectroscopy is given in Section 5. The criterion to separate strong from weak $H\alpha$ detections and from undetected targets is described in Section 6. The results are presented and discussed in Sections 7. We adopt a flat Λ CDM cosmology with $\Omega_M = 0.3$, $\Omega_\Lambda = 0.7$ and $H_0 = 73 \text{ km s}^{-1} \text{ Mpc}^{-1}$. Magnitudes are given in the AB system.

2. Sample

The sample of ETGs analyzed in this work was extracted from the ATLAS^{3D} whole-sky catalog of 260 ETGs (see Figure 1). The selection criteria adopted by Cappellari et al (2011) for including objects in ATLAS^{3D} are that they belong to a volume-limited sample of 42 Mpc radius, are brighter than $M_k = -21.5$

mag, and have $-6^\circ < \delta < 64^\circ$. The selection criterion for including them in our investigation is purely positional, according to target visibility in March–April from the site of SPM (latitude = +31 deg). ETGs were selected in the range $10^h < R.A. < 16^h$; $0^\circ < Dec. < 35^\circ$; this contains the Virgo cluster. Of the 260 galaxies in the ATLAS^{3D} survey, 151 fall within these boundaries: 29 of them were observed in previous $H\alpha$ imaging campaigns, 4 were not observed because of bright stars in their vicinity, and the remaining 118 are the subject of current observational campaigns, as illustrated in Figure 1 (blue symbols). To fill in the morning hours, we selected 20 filler targets in the Coma and Hercules superclusters in 2016 (green symbols). They mainly contribute to the setup of the $H\alpha$ reduction procedure (see Section 4.1.) The selection of 147 of 260 ATLAS^{3D} targets does not bias the distribution of the selected galaxies for the morphological and the kinematical type. The morphological type mix in ATLAS^{3D} is 74% S0 and 26% E; in our sample the two percentages become 68% and 32%. In ATLAS^{3D}, 14% of the ETGs are slow rotators (SR), and the remaining 86% are fast rotators (FR); in our sample the two percentages become 17% and 83%. However, the observed sample contains the Virgo cluster and is more biased in favor of cluster galaxies (52 %) than the entire ATLAS^{3D} survey (29 %).

3. Imaging observations

Narrow-band imaging of the $H\alpha$ line emission (rest frame $\lambda = 6562.8 \text{ \AA}$) of 118 galaxies in the main program (+ 20 filler targets) was obtained using the 2.1m telescope at the SPM, belonging to the Mexican Observatorio Astronómico Nacional (OAN). The $H\alpha$ measurements of the remaining 29 targets included in the present investigation are taken from the literature. The observations were scheduled in two observing runs of eight nights each in 2015 (March 17–24) and 2016 (April 7–14), both including new-moon periods. The weather phenomenon el Niño on the Pacific caused both runs to be severely affected by bad weather. In 2015, in particular, four nights were clear, and only 1.5 of them were photometric. In 2016 we worked in nearly photometric conditions during five nights out of eight. In both years, the Marconi CCD type e2vm2 was used with 2048x2048 pixel, binned twice with a pixel scale of 0.35 arcsec in a field of view of 5.5x5.5 arcmin. Each galaxy was observed using a narrow-band interference filter, whose bandpass included the redshifted wavelength of the $H\alpha$ line and also the [NII] lines (ON-band frame). These filters maximize the throughput at the galaxy redshift (see Fig. 2)¹. For each galaxy, we acquired three ON-band exposures with an integration time ranging from 5 to 10 min, according to the seeing conditions and source brightness. The stellar continuum subtraction was secured by means of shorter (typically three times 1 min) exposures taken through a broad-band ($\lambda 6231 \text{ \AA}$, $\Delta\lambda \sim 1200 \text{ \AA}$) *r*-Gunn filter (OFF-band frames).

While the median seeing of the SPM site is $\sim 0''.6$, the final FWHM for point sources in the images is affected by the poor telescope guiding and dome seeing. The final distribution ranges

¹ The transmission profiles of the interferometric filters plotted in Figure 2 refer to their nominal values, as measured in 2000 at 20 degrees Celsius. The transmission, however, is known to drift toward the blue by approximately 1 Å per 3 degrees Celsius. The filter transmission is also known to change slightly with time and to migrate toward the blue with beam convergence. These last two effects were not taken into account when we computed the transmissivity at the galaxy redshift. They should be negligible, however, given the F8.5 focal ratio of the 2.1m telescope.

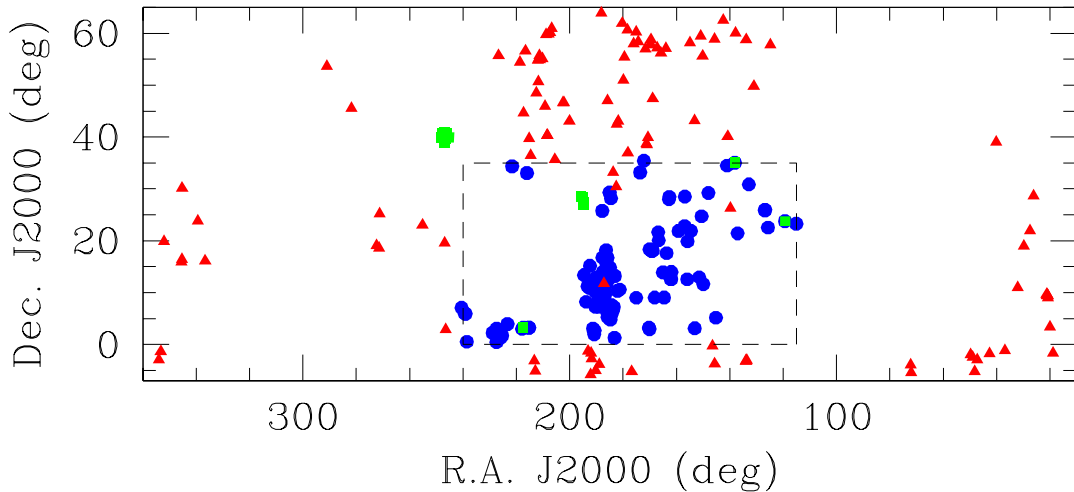


Fig. 1. Full ATLAS^{3D} survey (red triangles) and the subsample of 147 targets observed in $H\alpha$ as part of this work (blue circles). Green squares represent the 20 filler targets (not in ATLAS^{3D}).

from $\sim 1''$ to $\sim 2''$, with a mean seeing of $1''.20 \pm 0''.02$ in 2015 and $1''.50 \pm 0''.02$ in 2016, as shown in Fig. 3².

4. Data reduction

We reduced the CCD frames following the procedure described in Gavazzi et al. (2012), based on the STSDAS and GALPHOT IRAF packages. We refer to that paper for details and give here only a brief summary of the data reduction procedures. The methods for extracting the photometry of the $H\alpha$ + [NII] line (flux and equivalent width) and for estimating its error budget can also be found in Section 4.2 of Gavazzi et al. (2012).

In short, each image was bias-subtracted and flat-field corrected using sky exposures obtained during twilight in sky regions devoid of stars. When three exposures on the same object were available, we adopted a median combination of the realigned images to help reject the cosmic-ray hits in the final stack. Otherwise, we removed cosmic rays by direct inspection of the frames. We subtracted a mean sky background, computed around the galaxy, using the GALPHOT tasks MARKSKY and SKYFIT. The flat-fielded ON-frames were aligned with the OFF-frames using field stars. At this stage, the seeing was determined independently on the two sets of images. After normalization of the OFF-band frames (see Section 4.1), NET images were produced by subtracting the OFF from the ON-frames.

Given the high Galactic latitude of the observed sample, no flux correction for Galactic extinction was applied. We did not attempt deblending of $H\alpha$ from [NII] lines either, and no cor-

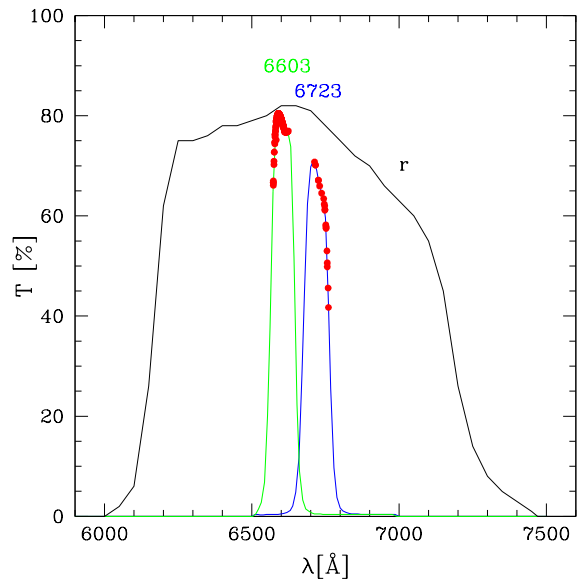


Fig. 2. Transmission profiles of the narrow-band filters (6603 Å: green line; 6723 Å: blue line) and of the r -band filter (black line). The observed galaxies (red dots) are overlaid on the narrow-band filter profiles at the wavelength given by their redshift.

² The sky-subtracted $H\alpha$ NET and OFF-band (normalized r) images are made available via the <http://goldmine.mib.infn.it/> site. The ON-band image can be obtained by adding the NET to the OFF image. The adopted photometric zero-point of the $H\alpha$ images and the seeing are stored in the headers.

rection for internal extinction was applied. The corrections computed with the scaling relations given in Section 4.3 of Gavazzi et al. (2012) refer to spiral galaxies, therefore they do not necessarily apply to our sample of ETGs. When we refer to $H\alpha$ measurements in the following, we mean $H\alpha$ + [NII], uncorrected for internal dust extinction.

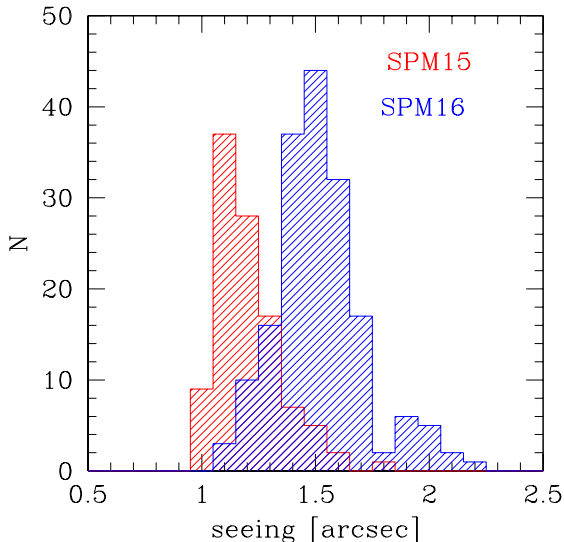


Fig. 3. Seeing conditions in 2015 (red) and 2016 (blue) measured on the final images. On average, the seeing in 2015 was 1.2 arcsec, while in 2016 it was 1.5 arcsec.

4.1. Calibrations

We calibrated the absolute flux scale using the standard stars Feige34, HZ44, and BD33 from the catalog of Massey et al. (1988), observed approximately every two hours. As shown in Figure 4, where the log of Zero Point (ZP) (in $\text{erg cm}^{-2}\text{sec}^{-1}$) is displayed, only night 7 and the first part of night 8 in 2015 can be considered photometric. For this reason, except for these two periods, most targets observed in 2015 were reobserved in 2016. Conversely, the 2016 run was clear in all five observable nights, with an acceptable uncertainty of 5 % on the zero-point.

4.2. Second-order calibration

Owing to the photometric instability in 2015 and because of the full-sky coverage of the SDSS survey (York et al. 2000), we checked and corrected the calibration of our r -band images by comparing the photometry of stars in each field with their SDSS magnitudes. Using the SDSS navigator tool, we inspected each target field and identified at least ten stars, five bluer and five redder than approximately $g - r = 0.8$ mag. For these stars we compared the SDSS r mag with the one measured in our r frames assuming the ZP derived for that night from the calibration stars. For each field we separately computed the median $g - r$ of the five blue and five red stars so that for each field, only two median measurements were considered. The median difference between the two sets of magnitudes (K_R) is plotted in Figure 5 as a function of the star color ($g - r$). While most measurements taken in 2016 appear to be accurate, we confirm the presence of few non-photometric measurements taken in 2015. We fit the 2016 data and used the ratio of the individual data taken in 2015 to the 2016 fit to determine the correct K_R coefficient. A similar method was used to check and correct the calibration of the ON-band data taken through the narrow-band filters.

In ideal conditions, the flux ratio of field stars should reflect the ratio in filter width combined with the ratio of integration time. In our case, the width ratio between our r -band filter and the narrow-band filters is approximately 11.5 (we compen-

sated for this large difference by adopting an approximately five times longer integration time for the ON-band observation). As remarked by Spector et al. (2012), however, the normalization factor ($K_{H\alpha}$) depends on the color of the stars, and the $K_{H\alpha}$ coefficient to be adopted should correspond to the actual color of the target galaxy (in our case, for ETGs $g - r \sim 0.8$), as illustrated in Figure 5. By applying this method we were able to improve the calibration for both the r band and the $H\alpha$ filters for the 118 observed galaxies.

A check of the quality of our flux calibration is performed in Figure 6, where we compare the $H\alpha + [\text{NII}]$ flux measured in this work with the value reported in the literature by Trinchieri & di Serego Alighieri (1991) and by Macchetto et al. (1996) for 13 galaxies in common (mostly upper limits). Nine of them are in good agreement, while two show discrepancies by one order of magnitude.

As a final test, we plot in Figure 7 a comparison between the flux (left panel) and the equivalent width (E.W.) (right panel) derived in our imaging data (separately for strong (blue) and weak (green) detections (see Section ??), including the 20 filler targets) by integrating the signal in a circular region of 3 arcsec diameter, with the values measured in the available nuclear spectra ($H\alpha + [\text{NII}]$), showing a satisfactory agreement. The nuclear spectra were taken from SDSS (DR13) when available, or from the NED (for the most part taken from Ho et al. 1995). The remaining 36 targets were observed by us using the Loiano 1.5m telescope, as described next. These are plotted only in the right panel of Figure 7, as they were not flux calibrated.

Because of the intrinsic shape of ETGs, namely their featureless $H\alpha$ emission, it is often difficult to assess the robustness of the $H\alpha$ emission associated with them based on the inspection of the NET images. NET frames result from the subtraction of ON-OFF images, both containing bright cuspy structures. Small variations in the seeing conditions combined with slightly (a few percent) imprecise determinations of the normalization coefficient can affect the resulting NET image. Buson et al. (1993) and Macchetto et al. (1996) adopted a strategy for adjusting the normalization coefficient that was based on the absence of negative NET residuals in the external parts of the galaxies themselves. Buson et al. (1993) in particular observed a sample of ETGs previously known for having some $H\alpha$ emission. The authors therefore adjusted the continuum subtraction up to the point that some $H\alpha$ residual remained in the NET image, without producing negative residuals in the outer parts. More quantitative, but based on a similar strategy, was the criterion adopted by Michielsen et al. (2004). These authors measured the ON-band and OFF-band flux in a elliptical corona fit to the galaxy periphery (between two fixed surface brightness levels) and set the normalization coefficient so that the two values were identical. These two criteria assume that no $H\alpha$ emission is present in the external regions of ETGs. We preferred not to adopt such a priori criterion, but to use many field stars to set the normalization coefficient, as described above.

5. Spectroscopic observations

Spectroscopic observations of 36 targets were found neither in the SDSS spectroscopic catalog nor in FITS form within the NED database. These nuclear spectra were obtained by us during several observing runs between 2013 and 2017 using the Bologna Faint Object Spectrograph and Camera (BFOSC, Gualandi & Merighi 2001) mounted on the 152 cm F/8 Cassini Telescope located in Loiano, belonging to the Observatory of Bologna. Similarly to previous observations at Loiano (Gavazzi

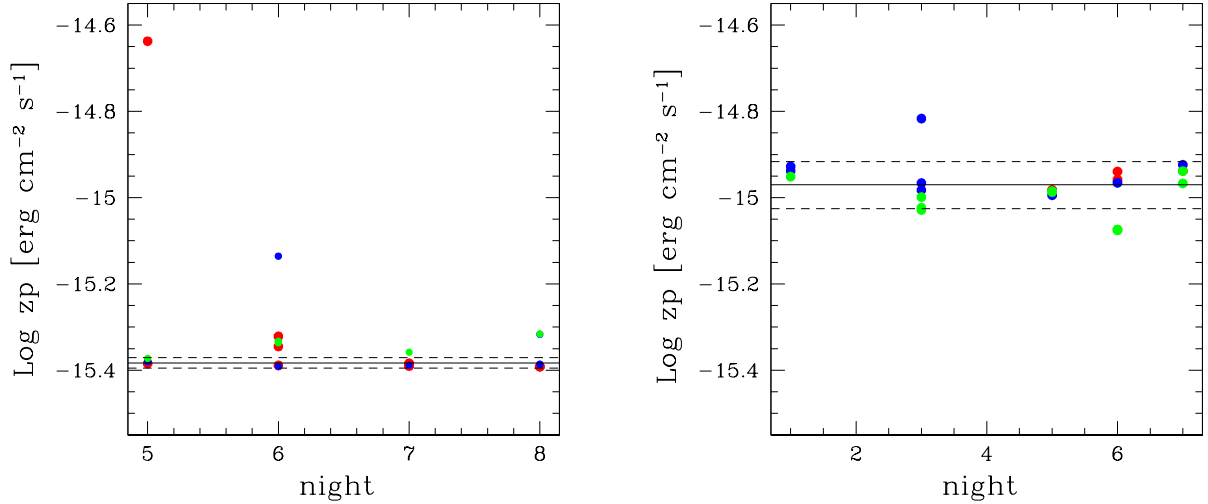


Fig. 4. Log of the photometric ZP (in $\text{erg cm}^{-2}\text{sec}^{-1}$) in 2015 (left) and 2016 (right), separately for the stars BD33 (blue), HZ44 (green), and FG34 (red). The dashed lines show the 1σ error bars computed using only the photometric periods in 2015 (night 7 and part of night 8) and all measurements taken in 2016.

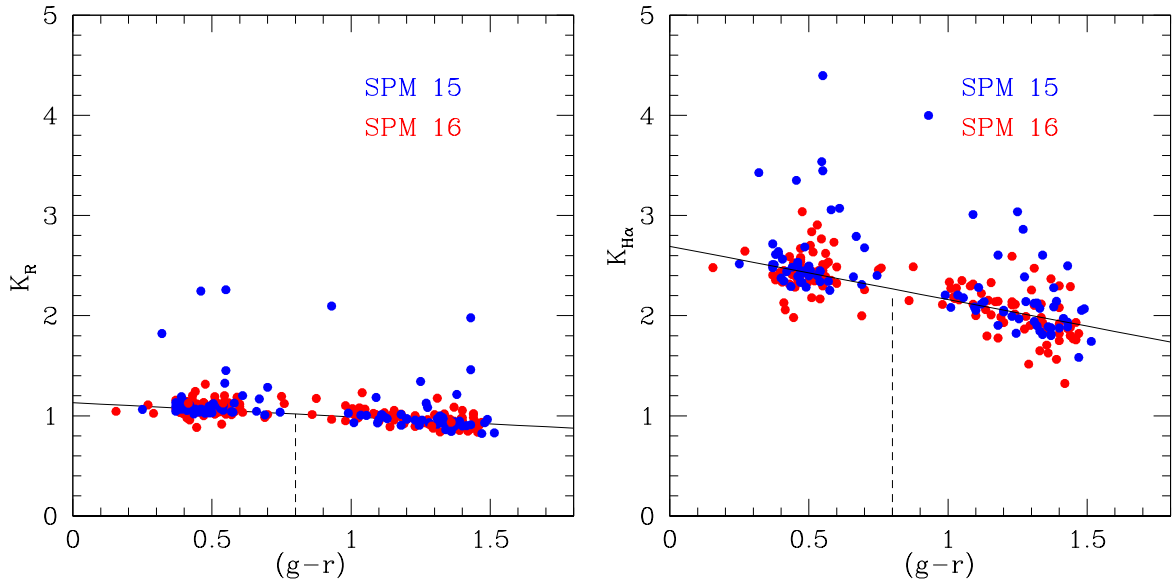


Fig. 5. (Left panel) Flux ratio K_R in r band between SDSS and this work plotted as a function of $g - r$ color of stars in the field. The 2016 data are plotted in red and the 2015 data in blue, including some non-photometric measurements. These can be corrected for using the 2016 fit by adjusting their K_R coefficient to the value derived from the 2016 fit computed at $g - r = 0.8$ using the vertical dashed line drawn at $g - r = 0.8$, which intersects the best-fit relation of the 2016 data. (Right panel): same for the $K_{H\alpha}$ coefficient.

et al. 2011, 2013), we acquired long-slit spectra taken through a slit of 2 arcsec width and 12.6 arcmin length, combined with an intermediate-resolution red-channel grism ($R \sim 2200$) covering the 6100 - 8200 Å portion of the spectrum, which includes the $H\alpha$, [NII], and [SII] lines. BFOC is equipped with an EEV LN/1300-EB/1 CCD detector of 1300x1340 pixels, reaching 90% QE near 5500 Å. For the spatial scale of 0.58 arcsec/pixel and a dispersion of 8.8 nm/mm, the resulting spectra have a resolution of 1.6 Å/pix.

Exposures of 5-10 minutes were repeated typically three times (to remove cosmic-ray hits). The slit was generally set in the E-W direction, except when taken along the direction connecting two nearby objects that simultaneously fell in the slit. The wavelength calibration was secured by means of frequent exposures of a He-Ar hollow-cathode lamp and further refined using bright OH sky lines. The spectrograph response was obtained by daily exposures of the star Feige34. The typical seeing conditions at Loiano ranged from 1.5'' to 2.5''. The spectra taken at Loiano were not flux calibrated, and

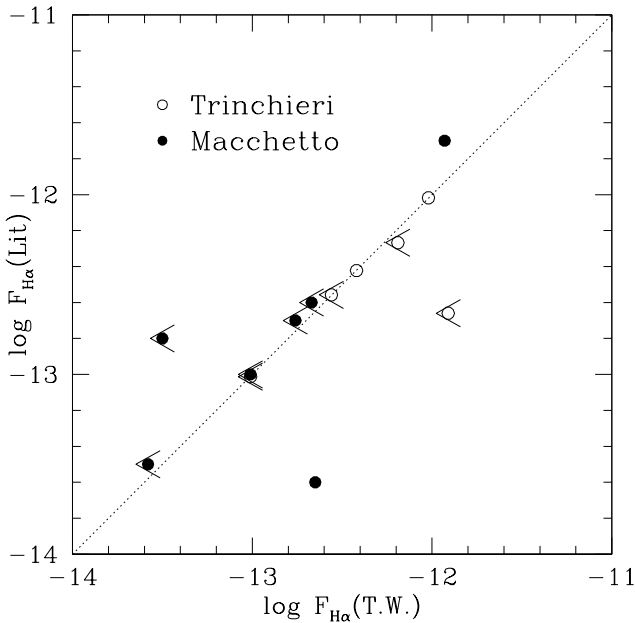


Fig. 6. Comparison of the $H\alpha$ + $[NII]$ flux measured in this work with the flux measured by Macchetto et al. (1996) and by Trinchieri & di Serego Alighieri (1991) for 13 galaxies in common. Only 4 objects were detected by us, the others are upper limits.

only measurements of the line EW were derived (right panel of Figure 7).

The spectra were reduced using standard IRAF procedures. After normalization to the flux in the interval 6400–6500 Å, they were shifted to λ_0 according to their redshift. Plots of the nuclear spectra obtained at Loiano, covering approximately from 6200 to 7200 Å, are given in Figure 11 in the Appendix.

6. Results

The detection threshold that we adopt in this paper comes from a combination of a flux and morphology criterion in the NET images: we considered detections all sources that have the global $H\alpha$ + $[NII]$ EW ≤ -1 Å (negative means emission), combined with $H\alpha$ + $[NII]$ $EW_{3\sigma} \leq -1$ Å, as determined in the central 3 arcsec aperture. To these sources, we added those (only three objects: M86 filamentary, NGC3156, and NGC4435 disk) that, while not meeting the $H\alpha$ EW thresholds, showed clear disc-like or filamentary structures in their NET images. Adopting these criteria, we detect 55 out of 147 galaxies. With a global detection rate of 39%, we find 21 strong detections with $H\alpha$ + $[NII]$ EW ≤ -5 Å, 34 weak detections with $-1 \leq EW < -5$ Å, and 92 undetected targets with $H\alpha$ + $[NII]$ EW > -1 .

$H\alpha$ continuum subtraction for weak $H\alpha$ emitters is subject to large errors. Colors may vary within galaxies (Spector et al. 2011). Continuum subtraction errors may therefore be relevant, especially for galaxies that are dominated by central emission (e.g., AGNs). We note that out of 34 weak candidate detections, a few (NGC2778, NGC4377, and NGC4551) could be spurious, as these galaxies show marginal global $H\alpha$ EW, have featureless $H\alpha$ morphology, and do not contain gas. Conversely, some undetected galaxies (NGC3379, NGC4281, and NGC5813) could be missed detections (on the basis of their gas content and/or

	S0 %	E %	$H\alpha$ d %	HSTd %	GAS %	AGN %	PAS %	HII %
Strong	76	24	47	57	43	24	24	52
Weak	63	36	27	53	9	50	50	0
Undetected	67	32	-	4	0	9	86	0

Table 1. Separately for the 21 strong and 34 weak $H\alpha$ detections and for the 92 undetected targets, we give the fraction of S0 and E optical morphology, the percentage of objects with an evident disc in their $H\alpha$ morphology, disc or dust in the HST images, the percentage of HI-H2 detections, the fraction of AGN, and passive or HII region-like nuclei.

disk morphology in the HST images). Even among the 21 strong detections, two (NGC4429 and NGC4550) might be partly contaminated by imperfect continuum subtraction (see Figure 12). Nevertheless, three missing and five spurious detections would not change the conclusions of the present investigation. We also note that half (50%) of the weak sources are AGNs (or LIN). This means that their nuclear spectrum is dominated by $[NII]$ rather than by $H\alpha$, and they therefore do not contribute to their nuclear star formation (SFR) (e.g., Theios et al. 2016). For these objects, the SFRs given in Table 7 must be considered as upper limits.

The NET and OFF images of the 14 galaxies with strong $H\alpha$ emission observed in this work are given in grayscale in Figure 12 in the Appendix. We note that the ON- and normalized OFF-images were not convolved to the same resolution before subtraction to produce NET images free from seeing effects. This is made possible by our strategy of observing the ON and OFF frames not only in the same night, but also within minutes from one another.

Table 1 reports separately for the strong and weak $H\alpha$ detections and for the undetected targets the fraction of objects for each optical morphological class, the fraction of conspicuous $H\alpha$ discs and/or dusty structures in the HST images, the fraction of gas-rich (HI or CO detected) objects and the fraction of AGN, passive and HII region-like nuclei from spectroscopy. Strong detections appear associated mainly with S0 gas-rich galaxies, with $H\alpha$ and HST discs, and for the most part, they harbor HII region-like nuclei. AGNs are overabundant among the weak sources. This implies that the emission in this class of sources is not due to star formation associated with the $H\alpha$ line, but to relatively strong $[NII]$. Moreover, undetected targets are gas-free, disk-free systems without star formation, neither extended nor nuclear, without abundant AGNs, but with passive nuclear spectra.

The strong $H\alpha$ emitters ($H\alpha EW < -5$ Å) are significantly (11/21: 52%) associated with HII region-like spectra. Conversely, 19 of 34 are weak $H\alpha$ emitters ($-1 \leq EW < -5$ Å): 55% are AGN, and 15 of 34: 44% are passive (PAS) or retired (RET), none HII.

For the environmental dependence of the ETG properties, we recall that Cappellari (2016) reported that slow rotators constitute a significant fraction only in the centers of cluster and groups. Our subsample of ATLAS^{3D} comprises the entire Virgo cluster, therefore we can check whether the fraction of detected and undetected galaxies also correlates with the projected distance from M87. We find that 38% of the strong detected galaxies and 58% of the undetected galaxies are found inside the Virgo cluster, hinting at a marginal environmental anticorrelation between the ionized gas content (and star formation) and the projected galaxy density.

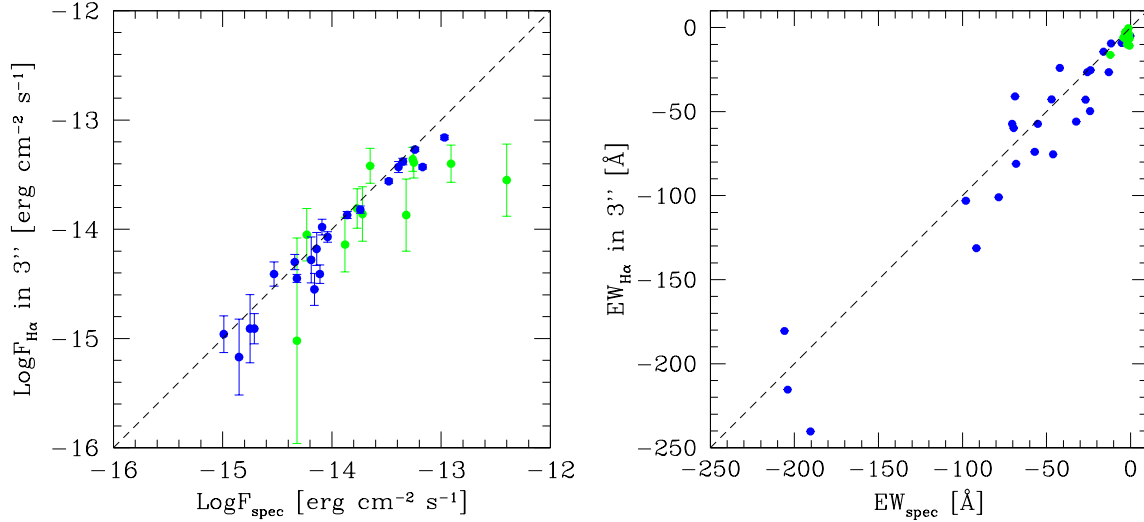


Fig. 7. Comparison between the $H\alpha$ + $[NII]$ flux (left) and E.W. (right) detected in the central 3 arcsec in the imaging data and in the nuclear spectra. The right panel includes the 36 spectra taken at Loiano. Blue are strong detections, and green are weak detections (the most discrepant object is N4526). The sources of observations of nuclear spectra are provided in Table 7. The 45-degree lines serve to guide the eye to the proportionality relations.

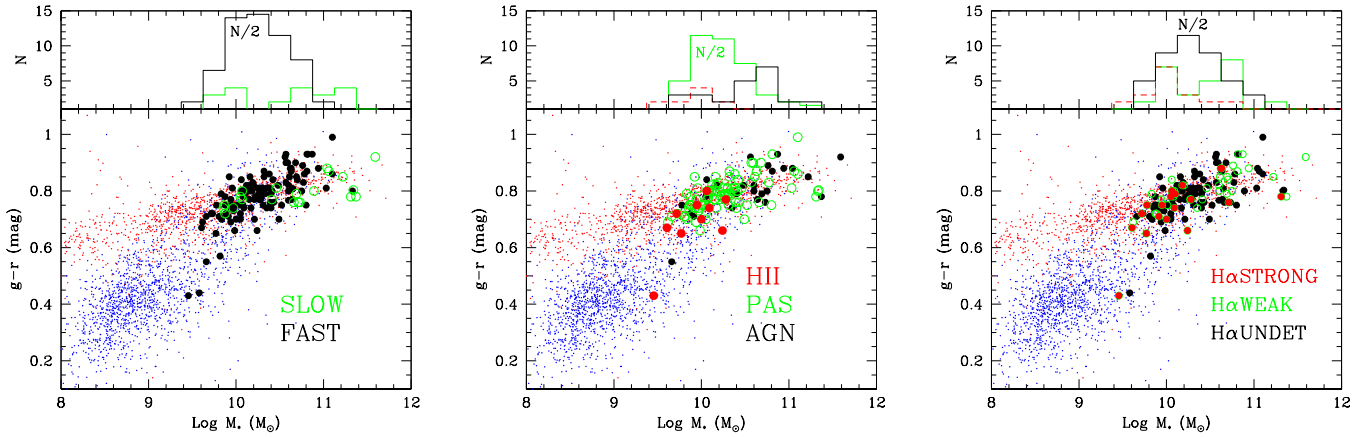


Fig. 8. Color-stellar mass relation for a complete sample of galaxies in the Coma and Local supercluster from Gavazzi et al. (2010) (small symbols), subdivided into ETGs (red) and LTGs (blue) to show the separation between the red and the blue sequence. (Left) The 32 slow-rotator (green open symbols) and the 222 fast-rotator (black filled symbols) ETGs from the whole ATLAS^{3D} survey (large symbols). (Center) The 41 AGNs (green open symbols) and the 165 passive (black filled symbols) ETGs from the whole ATLAS^{3D} survey (large symbols). (Right) The 22 strong (red), 33 weak (green open symbols), and the 92 undetected (black filled symbols) ETGs from the ATLAS^{3D} survey (large symbols).

To show that ATLAS^{3D} targets are genuine red sequence systems, with only little contamination from blue cloud and green valley objects, we plot in Figure 8 the color ($g-r$) versus stellar mass (M_{\odot}) relation for the full ATLAS^{3D} sample (large symbols), while in the same figure we plot (small symbols) the color-luminosity relation from a complete sample of SDSS galaxies in the Coma supercluster (selected and morphologically classified by Gavazzi et al. 2010), separately for LTGs (blue) and ETGs (red).

In Figure 8 (left panel) we first confirm a result that is known from Emsellem et al. (2011), who showed that slow rotators tend to be massive ($M_{dyn} > 10^{10.5} M_{\odot}$) and dominate the high-mass end of ETGs. This result has been emphasized by Veale et al. (2017), who showed that the fraction of slow rotators, that is, a

mere 14 % in the ATLAS^{3D} survey, reaches 90% for the massive ($M_{dyn} > 10^{10.5} M_{\odot}$) ETGs ($M_K < -26$ mag). For example, the brightest ATLAS^{3D} members of the Virgo cluster that are included in our work (N4472=M49, N4486=M87, N4374=M84, and N4406=M86) are all slow rotators (see also Boselli et al. 2014). In agreement with Emsellem et al. (2011), we interpret this result as an indication that massive slow rotators represent the extreme instances within the red sequence of galaxies that might have suffered from significant merging without being able to rebuild a fast-rotating component.

Figure 8 (central panel) gives the color-mass relation, dividing galaxies with respect to their nuclear spectral classification

according to Gavazzi et al. (2011, 2013)³. AGNs (SEY+AGN) are plotted separately from passive (PAS+LIN+RET) and from HII-like systems. Again there is a significant separation between the average luminosity of AGNs, which are brighter than PAS by 0.6 mag on average. This result is expected (see, e.g., Gavazzi et al. 2011), and along with the previous finding, it helps explain why slow rotators in ATLAS^{3D} contain a larger fraction of AGNs (31%) than fast rotators (13%). Conversely, HII region-like nuclei are harbored by the least massive galaxies, but the small statistics prevents us from being more quantitative. The frequency of AGNs is 30% among galaxies more massive than $10^{10.5} M_{\odot}$, which is significantly higher than the 10% found among galaxies less massive than $10^{10.5} M_{\odot}$. These values are consistent with those of Kauffmann et al. (2003b), who found that galaxies with $10^{10.5} M_{\odot}$ harbor between 20% and 40% of AGNs. They also found that the fraction of AGNs among emission-line galaxies increases steeply with mass, reaching 100% when the stellar mass reaches $10^{11.5} M_{\odot}$.

In order to understand the difference between ETGs that are detected in $H\alpha$ from the undetected ones, we plot in Figure 8 (right panel) the color-mass relation for the subsample of 147 ATLAS^{3D} observed in $H\alpha$, subdivided between detected (strong or weak) and undetected objects. Significant mass segregation is evident. Weak detections are spread over the entire mass range, and the most massive objects coincide with slow-rotating AGNs. The strong detections are associated with low-mass systems, which from the previous analysis were identified with HII region-like nuclei. These are associated with S0 galaxies and tend to avoid Es.

In Figure 9 we compare the SFR derived for a set of galaxies in the HRS catalog of Boselli et al. (2015; mainly composed of LTGs) with the SFR obtained for ETGs in this work (limited to the 55 galaxies detected in our $H\alpha$ imaging campaign). It is clear that LTGs have, for any given stellar mass, an SFR higher by about a factor of 20 than ETGs, and that ETGs in our survey agree well with the few ETGs in the HRS survey.

The relation between the frequency of $H\alpha$ detections and the gaseous content (HI or H₂; Figure 10) shows an obvious correlation: of the 55 $H\alpha$ detected ETGs, 33 (60%) are found to retain gas. On the other hand, only 7 (8%) of the 92 undetected ETGs have gas. However, when considering the 12 detected objects that have positive HI and H₂ detections (we note that 11 of them are S0 and only 1 is an E), we find a barely significant correlation between the total (HI+H₂) gas mass and the $H\alpha$ luminosity (see the red symbols in Figure 10). When we overplot the relation between the similar quantities for a sample of 131 LTGs from the *Herschel* Reference Sample by Boselli et al. (2010) that have been detected in $H\alpha$ (Boselli et al. 2015) and in HI and CO (Boselli et al. 2014b), we find that the ETG population is consistent with the low-mass tail of LTGs. We note that of the 12 detected ETGs with gas in Figure 10, 6 have HII region-like nuclear spectra, indicating that star formation is occurring in their nuclei. The other 6 are AGNs of some kind. Furthermore, 8 are galaxies with a relatively strong $H\alpha$ luminosity and an EW and gaseous content. The 4 objects with the lowest luminosity and gas content are members of the Virgo cluster (within 7 degrees of the projected angular separation from M87).

³ Gavazzi et al. (2011) classified the nuclear spectra by dividing them into HII region-like, strong AGNs (including SEY), liners (LIN), "retired" nuclei (RET) that are likely excited by old stars, and passive nuclei (PAS).

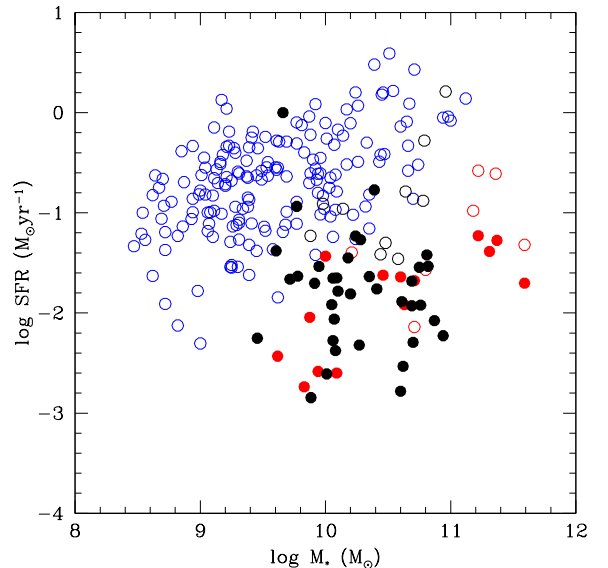


Fig. 9. Relation between the stellar mass and the SFR separately for a set of HRS galaxies (empty symbols): (blue: LTG, black: S0+S0a, and red: E) and the ETGs from this work (filled symbols): red: E, and black: S0.

To assess the comparison of the ETGs with the LTGs from HRS in the $H\alpha$ luminosity/dust mass plane, we cross-correlated the HRS catalog (Ciesla et al. 2014) with the ATLAS^{3D} sample of 147 ETGs observed by us in $H\alpha$, finding 11 matches. In Figure 11 we plot (with similar symbols as in Figure 10) the relation between $H\alpha$ luminosity and dust mass for 214 LTGs detected at 22 micron by WISE and at 250 micron by SPIRE on board *Herschel*, providing an estimate of the dust mass. It is again evident that the 11 ETGs do not deviate significantly from the sequence occupied by LTGs.

The majority of ATLAS^{3D} targets have been observed with HST, providing high-resolution optical images. Many of them appear to harbor a distinct disc structure at their interior. Interestingly, 30 of 55 (55%) of the detected ETGs show evidence of structures (disc or dust filaments) in the HST images. Conversely, only 4 (4%) of the 92 undetected ETGs have similar structures. Eight of 12 gas-rich ETGs show dusty discs in the HST images. The galaxy morphological mix in the observed sample is 68% S0s versus 32% Es. In the detected galaxies this mix does not change at all: 68% S0s and 32% Es.

When we divide the galaxies into $H\alpha$ detected and undetected, these ratios change as follows: of the detected galaxies, 32 of 55 (58%) are AGN of various types, 11 of 55 (20%) are HII regions, and 12 of 55 (22%) are PAS. Of the undetected galaxies, 13 of 92 (14%) are AGN of various types, none of the 92 (0%) are HII regions, and 74 of 92 (80%) are PAS. To summarize, the relative majority of detected galaxies are AGNs, while the relative majority of the undetected galaxies are PAS.

7. Conclusions and summary

We have analyzed $H\alpha$ imaging observations of 147 early-type galaxies selected from the (260) targets in the ATLAS^{3D} catalog, assumed to be representative of the ETG population in the local Universe. For the totality of our sample, we also gathered nuclear spectroscopy, either from the literature, or by new observations (36 objects), allowing their nuclear classification. Fifty-

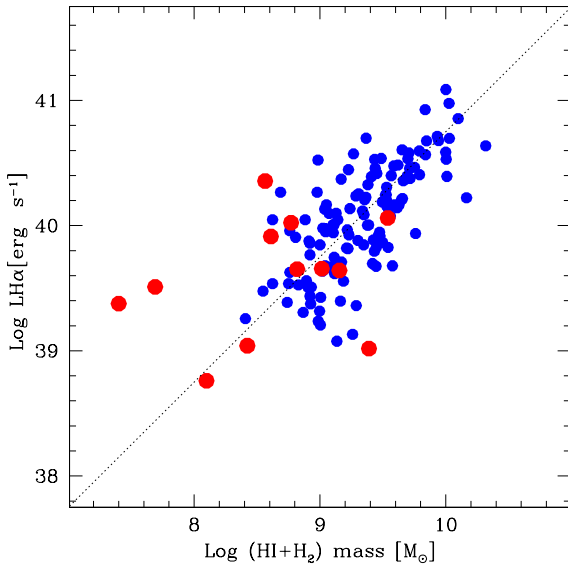


Fig. 10. Relation between the gas (HI+H₂) mass and the H α luminosity separately for a set of 131 LTGs from HRS (blue) and 12 ETGs from this work (red). The dotted line is to guide the eye on the direct proportionality relation.

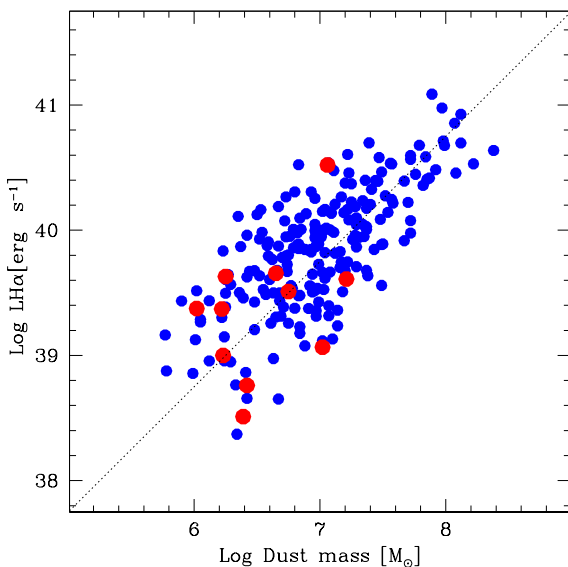


Fig. 11. Relation between the dust mass and the H α luminosity separately for a set of 214 LTGs from HRS (blue) and 11 ETGs from this work (red). The dotted line is to guide the eye on the direct proportionality relation.

five ETGs (37%) were detected as H α emitters above our threshold limit ($H\alpha$ $EW \leq -1$ Å), and 21 were above $H\alpha$ $EW \leq -5$ Å. Seventy-six percent of the strong emitters were found to be associated with low-mass ($M_* \sim 10^{10} M_\odot$) S0 galaxies, showing a conspicuous gas (HI+H₂) content, extended stellar disks, and star formation even in their nuclei. All but two of them are fast rotators. The remaining 33 weak detections were found to be associated with more massive ($M_* \sim 10^{11} M_\odot$) gas-poor targets that often harbor an AGN in their nucleus. Two-thirds of them are fast rotators and 64% are associated with S0 galaxies. The majority of the remaining (92) undetected systems are gas poor

and diskless and show a passive spectrum even in their nucleus. Eighty-eight percent of them are associated with fast rotators and 66% with S0 galaxies.

These pieces of evidence, considered in the light of the cinematic measurements provided by ATLAS^{3D} (Cappellari, 2016), reinforce the evolutionary picture where the majority of the current low-mass ETGs are in fact the outcome of a secular evolution of diskly gas-rich systems governed by rotation and star formation, both on the disc and on the nuclear scale. In contrast, the most massive ($M_* > 10^{10.5} M_\odot$) ETGs are genuine products of dry merging, which dissipated their angular momentum, and they provide the evolutionary track of giant galaxies at the center of rich clusters of galaxies.

Acknowledgements. This research has made use of the GOLDmine database (Gavazzi et al. 2003, 2014b) and of the NASA/IPAC Extragalactic Database (NED) which is operated by the Jet Propulsion Laboratory, California Institute of Technology, under contract with the National Aeronautics and Space Administration. Funding for the Sloan Digital Sky Survey (SDSS) and SDSS-II has been provided by the Alfred P. Sloan Foundation, the Participating Institutions, the National Science Foundation, the U.S. Department of Energy, the National Aeronautics and Space Administration, the Japanese Monbukagakusho, and the Max Planck Society, and the Higher Education Funding Council for England. The SDSS Web site is <http://www.sdss.org/>. The SDSS is managed by the Astrophysical Research Consortium (ARC) for the Participating Institutions. The Participating Institutions are the American Museum of Natural History, Astrophysical Institute Potsdam, University of Basel, University of Cambridge, Case Western Reserve University, The University of Chicago, Drexel University, Fermilab, the Institute for Advanced Study, the Japan Participation Group, The Johns Hopkins University, the Joint Institute for Nuclear Astrophysics, the Kavli Institute for Particle Astrophysics and Cosmology, the Korean Scientist Group, the Chinese Academy of Sciences (LAMOST), Los Alamos National Laboratory, the Max-Planck-Institute for Astronomy (MPIA), the Max-Planck-Institute for Astrophysics (MPA), New Mexico State University, Ohio State University, University of Pittsburgh, University of Portsmouth, Princeton University, the United States Naval Observatory, and the University of Washington. M. Fossati acknowledges the support of the Deutsche Forschungsgemeinschaft via Project ID 387/1-1. M. Fumagalli acknowledges support by the Science and Technology Facilities Council [grant number ST/P000541/1].

References

- Abazajian, K. N., Adelman-McCarthy, J. K., Agüeros, M. A., et al. 2009, *ApJS*, 182, 543-558
- Alam, S., Albareti, F. D., Allende Prieto, C., et al. 2015, *ApJS*, 219, 12
- Albareti, F. D., et al. 2016, preprint
- Baldry, I. K., Glazebrook, K., Brinkmann, J., et al. 2004, *ApJ*, 600, 681
- Balogh, M. L., Baldry, I. K., Nichol, R., et al. 2004, *ApJ*, 615, L101
- Belfiore, F., Maiolino, R., Maraston, C., et al. 2016, *MNRAS*, 461, 3111
- Bell, E. F., McIntosh, D. H., Katz, N., & Weinberg, M. D. 2003, *ApJS*, 149, 289
- Bois, M., Emsellem, E., Bournaud, F., et al. 2011, *MNRAS*, 416, 1654
- Boselli, A., & Gavazzi, G. 2002, *A&A*, 386, 124
- Boselli, A., & Gavazzi, G. 2006, *PASP*, 118, 517
- Boselli, A., Eales, S., Cortese, L., et al. 2010, *PASP*, 122, 261
- Boselli, A., Hughes, T. M., Cortese, L., Gavazzi, G., & Buat, V. 2013, *A&A*, 550, A114
- Boselli, A., & Gavazzi, G. 2014, *A&A Rev.*, 22, 74
- Boselli, A., Fossati, M., Gavazzi, G., et al. 2015, *A&A*, 579, A102
- Boselli, A., Voyer, E., Boissier, S., et al. 2014, *A&A*, 570, A69
- Boselli, A., Cortese, L., & Boquien, M. 2014, *A&A*, 564, A65
- Boselli, A., Fossati, M., Gavazzi, G., et al. 2015, *A&A*, 579, A102
- Bryant, J. J., Owers, M. S., Robotham, A. S. G., et al. 2015, *MNRAS*, 447, 2857
- Buson, L. M., Sadler, E. M., Zeilinger, W. W., et al. 1993, *A&A*, 280, 409
- Cappellari, M., Emsellem, E., Krajnović, D., et al. 2011, *MNRAS*, 413, 813
- Cappellari, M., Emsellem, E., Krajnović, D., et al. 2011, *MNRAS*, 416, 1680
- Cappellari, M. 2016, *ARA&A*, 54, 597
- Ciesla, L., Boquien, M., Boselli, A., et al. 2014, *A&A*, 565, A128
- Consolandi, G., Gavazzi, G., Fumagalli, M., Dotti, M., & Fossati, M. 2016, *A&A*, 591, A38
- di Serego Alighieri, S., Gavazzi, G., Giovanardi, C., et al. 2007, *A&A*, 474, 851
- Emsellem, E., Cappellari, M., Krajnović, D., et al. 2011, *MNRAS*, 414, 888
- Gavazzi, G., Boselli, A., Vílchez, J. M., Iglesias-Paramo, J., & Bonfanti, C. 2000, *A&A*, 361, 1

night	2015		2016	
	obs	obs.cond.	obs.	obs.cond.
1	N	-	Y	P
2	N	-	N	-
3	N	-	Y	P
4	N	-	N	-
5	Y	nP	Y	P
6	Y	nP	Y	P
7	Y	P	Y	P
8	Y	P/nP	N	-
Log Zero-point				
		-15.29 ± 0.03	-14.97 ± 0.05	

Table 2. Separately for the 2015 and 2016 runs, we list the usable nights and the photometric quality (P=photometric; nP= not photometric). The average ZPs with uncertainty are given in the last line. The 0.3 dex difference between the two ZPs derives from a different setup of the CCD readout electronics.

- Gavazzi, G., Boselli, A., Pedotti, P., Gallazzi, A., & Carrasco, L. 2002, A&A, 386, 114
- Gavazzi, G., Boselli, A., Donati, A., Franzetti, P., & Scodreggio, M. 2003, A&A, 400, 451
- Gavazzi, G., Savorgnan, G., & Fumagalli, M. 2011, A&A, 534, A31
- Gavazzi, G., Fumagalli, M., Cucciati, O., & Boselli, A. 2010, A&A, 517, A73
- Gavazzi, G., Fumagalli, M., Galardo, V., et al. 2012, A&A, 545, A16
- Gavazzi, G., Consolandi, G., Dotti, M., et al. 2013, A&A, 558, A68
- Gavazzi, G., Consolandi, G., Dotti, M., et al. 2015, A&A, 580, A116
- Grossi, M., di Serego Alighieri, S., Giovanardi, C., et al. 2009, A&A, 498, 407
- Gualandri R., & Merighi, R. Thecnical report 2001, Bologna Astronomical Observatory
- Ho, L. C., Filippenko, A. V., & Sargent, W. L. 1995, ApJS, 98, 477
- Kenney, J. D. P., Tal, T., Crawl, H. H., Feldmeier, J., & Jacoby, G. H. 2008, ApJ, 687, L69
- Kauffmann, G., White, S. D. M., & Guiderdoni, B. 1993, MNRAS, 264, 201
- Kauffmann, G., Heckman, T. M., White, S. D. M., et al. 2003, MNRAS, 341, 54
- Kauffmann, G., Heckman, T. M., Tremonti, C., et al. 2003b, MNRAS, 346, 1055
- Kennicutt, R. C., Jr. 1998, ARA&A, 36, 189
- Kennicutt, R. C., Jr., & Kent, S. M. 1983, AJ, 88, 1094
- Kennicutt, R. C., Jr. 1992, ApJ, 388, 310
- Koopmann, R. A., Kenney, J. D. P., & Young, J. 2001, ApJS, 135, 125
- Koopmann, R. A., Haynes, M. P., & Catinella, B. 2006, AJ, 131, 716
- Koopmann, R. A., & Kenney, J. D. P. 2006, ApJS, 162, 97
- Macchetto, F., Pastoriza, M., Caon, N., et al. 1996, A&AS, 120, 463
- Massey, P., Strobel, K., Barnes, J. V., & Anderson, E. 1988, ApJ, 328, 315
- Michielsen, D., de Rijcke, S., Zeilinger, W. W., et al. 2004, MNRAS, 353, 1293
- Moore, B., Lake, G., Quinn, T., & Stadel, J. 1999, MNRAS, 304, 465
- Paturel, G., Petit, C., Prugniel, P., et al. 2003, A&A, 412, 45
- Penoyre, Z., Moster, B. P., Sijacki, D., & Genel, S. 2017, arXiv:1703.00545
- Sánchez, S. F., Kennicutt, R. C., Gil de Paz, A., et al. 2012, A&A, 538, A8
- Serra, P., Oosterloo, T., Morganti, R., et al. 2012, MNRAS, 422, 1835
- Spector, O., Finkelman, I., & Brosch, N. 2012, MNRAS, 419, 2156
- Theios, R. L., Malkan, M. A., & Ross, N. R. 2016, ApJ, 822, 45
- Trinchieri, G., & di Serego Alighieri, S. 1991, AJ, 101, 1647
- Veale, M., Ma, C.-P., Thomas, J., et al. 2017, MNRAS, 464, 356
- Yıldız, M. K., Serra, P., Peletier, R. F., Oosterloo, T. A., & Duc, P.-A. 2017, MNRAS, 464, 329
- York, D. G., Adelman, J., Anderson, J. E., Jr., et al. 2000, AJ, 120, 1579
- Young, J. S., Allen, L., Kenney, J. D. P., Lesser, A., & Rownd, B. 1996, AJ, 112, 1903
- Young, L. M., Bureau, M., Davis, T. A., et al. 2011, MNRAS, 414, 940
- Zibetti, S., Charlot, S., & Rix, H.-W. 2009, MNRAS, 400, 1181

8. APPENDIX A

The logbook of the observations is provided in Table 2.

The 147 galaxies selected from ATLAS^{3D} for $H\alpha$ observations (either from this work or from the literature) are listed in Table 3, organized as follows:

- Column (1): galaxy name;
- Column (2) and (3): J2000 celestial coordinates;
- Column (4): recessional velocity in km/s;
- Column (5): assumed distance in Mpc;
- Column (6): morphological classification in ATLAS^{3D} (Cappellari et al. 2011);
- Column (7): SDSS magnitude in g from Consolandi et al. (2016);
- Column (8): SDSS magnitude in r from Consolandi et al. (2016);
- Column (9): log of stellar mass M_{star} computed by us from the r -band absolute magnitude and the $g-r$ color index using the prescription of Zibetti et al. (2009).
- Column (10): kinematic classification in ATLAS^{3D} (Emsellem et al. 2011) as fast (F) or slow (S) rotators;
- Column (11): log of the molecular hydrogen mass (H_2) in M_\odot with sign, as given by Young et al. (2011); when a CO spectrum is available from the NED, but an estimate of the H_2 mass is not given, a "H2" is reported.
- Column (12): log of the atomic hydrogen mass (HI) in M_\odot with sign, as given by Serra et al. (2012); when a HI spectrum is available from NED (mostly from ALFALFA), but an estimate of the HI mass is not given, a "HI" is reported.

The observational parameters of the target galaxies are given in Table 5 as follows:

- Column (1): galaxy name;
- Column (2): reference to the $H\alpha$ observation (see also Column 16 in Table 7);
- Column (3): air mass during the ON-band exposure in 2015;
- Column (4): air mass during the OFF-band exposure in 2015;
- Column (5): air mass during the ON-band exposure in 2016;
- Column (6): air mass during the OFF-band exposure in 2016;
- Column (7): exposure time (in seconds) of the individual ON-band exposure in 2015; three equal exposures were combined.
- Column (8): exposure time (in seconds) of the individual OFF-band exposure in 2015; three equal exposures were combined.
- Column (9): exposure time (in seconds) of the individual ON-band exposure in 2016; three equal exposures were combined.
- Column (10): exposure time (in seconds) of the individual OFF-band exposure in 2016; three equal exposures were combined.

The results of our $H\alpha$ imaging campaign are listed in Table 7, organized as follows:

- Column (1): galaxy name;
- Columns (2, 3): (EW) $H\alpha$ + [NII] (in Å) measured in a circular aperture of $3''$ positioned on the galaxy nucleus, with associated uncertainty;
- Columns (4, 5): log of the $H\alpha$ + [NII] flux ($\text{erg cm}^{-2} \text{s}^{-1}$) measured in a circular aperture of $3''$ positioned on the galaxy nucleus, with associated uncertainty;
- Columns (6, 7): total (EW) $H\alpha$ + [NII] (in Å) measured in a circular aperture containing the whole galaxy, with associated uncertainty;
- Columns (8, 9): total log of the $H\alpha$ + [NII] flux ($\text{erg cm}^{-2} \text{s}^{-1}$) measured in a circular aperture containing the whole galaxy, with associated uncertainty;
- Column (10): log of the total star formation rate derived from the $H\alpha$ flux as prescribed by Kennicutt (1998), but adapted for a Chabrier IMF.

Column (11): availability of a nuclear spectrum: LOI = taken at the Loiano 1.5m telescope (this work); SDSS = taken from the SDSS database; NED = taken from NED; HO= in Ho

et al. 1995; NEDMH= from NED taken at Mount Hopkins 1.5m telescope.

Column (12): nuclear spectral classification; HII, SEY, AGN, PSB, RET, PAS, according to the criteria of Gavazzi et al. (2012; 2013);

Column (13): 1=strong $H\alpha$ detection; 2=weak detection, 3=undetected.

Column (14): $H\alpha$ morphological classification; d=disc, D=diffuse, c=centrally peaked, F=filamentary;

Column (15): HST imaging availability: -: not available; 0: available, featureless; 1: available, showing a prominent structure (disc, dust ring, or filaments);

Column (16): reference to $H\alpha$ imaging. 1: this work; 2: Koopmann & Kenney (2006); 3: Boselli et al. (2015); 4: Young et al. (1996); 5: Macchetto et al. (1996); 6: Koopmann et al. (2001); 7: Boselli & Gavazzi (2002); 8: Kennicutt & Kent (1983); 9: Trinchieri & Di Serego Alighieri (1991); 10: Gavazzi et al. (2000), 11: Kenney et al. (2008).

Filler targets are listed in Table 4, their observational parameters are given in Table 6, and the photometric parameters are listed in Table 8.

Galaxy	RA J2000.0	Dec J2000.0	cz km/s	D Mpc	Type	g mag	r mag	logM _{star} M_{\odot}	Rot	log M(H ₂) M_{\odot}	log M(HI) M_{\odot}
UGC03960	07h40m22.75s	+23d16m30.0s	2255	33.2	E	14.06	13.31	-	S/F	<7.81	7.79
NGC2481	07h57m13.75s	+23d46m04.0s	2157	32.0	S0	13.29	12.36	10.57	F	<7.79	<7.42
NGC2577	08h22m43.45s	+22d33m11.1s	2062	30.8	S0	12.77	11.90	10.63	F	<7.71	<7.35
NGC2592	08h27m08.05s	+25d58m13.1s	1979	25.0	E	12.97	12.12	10.32	F	<7.54	<7.18
NGC2594	08h27m17.16s	+25d52m43.7s	2362	35.1	S0	14.12	13.27	10.16	F	<7.83	8.91
NGC2679	08h51m32.94s	+30d51m55.3s	2027	31.1	S0	13.55	12.80	10.08	F	<7.87	<7.35
NGC2764	09h08m17.47s	+21d26m36.0s	2706	39.6	S0	13.20	12.54	10.24	F	9.19	9.28
NGC2778	09h12m24.37s	+35d01m39.1s	2025	22.3	E	13.05	12.25	10.09	F	<7.48	<7.06
NGC2859	09h24m18.53s	+34d30m48.6s	1690	27.0	S0	11.82	11.02	10.75	F	<7.61	8.46
NGC2962	09h40m53.93s	+05d09m56.9s	1967	34.0	S0	12.81	11.88	10.82	F	<7.85	-
NGC3032	09h52m08.15s	+29d14m10.4s	1562	21.4	S0	12.99	12.34	9.77	F	8.41	8.04
PGC028887	09h59m43.49s	+11d39m38.7s	2833	41.0	S0	14.43	13.63	10.07	S/F	<8.03	7.65
NGC3098	10h02m16.69s	+24d42m39.9s	1397	23.0	S0	12.81	12.04	10.15	F	<7.47	<7.12
PGC029321	10h05m51.19s	+12d57m40.7s	2816	40.9	S0	14.89	14.14	9.78	F	8.53	<7.68
NGC3156	10h12m41.25s	+03d07m45.7s	1338	21.8	S0	12.79	12.24	9.66	F	7.67	-
NGC3193	10h18m24.90s	+21d53m38.3s	1381	33.1	E	11.62	10.81	11.03	F	<7.91	8.19
NGC3226	10h23m27.01s	+19d53m54.4s	1315	22.9	E	12.17	11.29	10.63	F	<7.41	<7.10
NGC3230	10h23m43.96s	+12d34m04.0s	2795	40.8	S0	12.82	11.83	11.10	F	<8.0	<7.71
NGC3245	10h27m18.39s	+28d30m26.8s	1326	20.3	S0	11.64	10.75	10.76	F	7.27	<7.00
NGC3248	10h27m45.44s	+22d50m49.9s	1481	24.6	S0	12.95	12.23	10.05	F	<7.55	<7.22
NGC3301	10h36m56.04s	+21d52m55.7s	1339	22.8	S0	12.22	11.40	10.48	F	<7.46	7.13
NGC3377	10h47m42.33s	+13d59m09.3s	690	10.9	E	-	-	-	F	<6.96	<6.52
NGC3379	10h47m49.59s	+12d34m53.8s	918	10.3	E	10.54	9.75	10.40	F	<6.72	<6.49
NGC3384	10h48m16.89s	+12d37m45.4s	733	11.3	S0	10.76	10.01	10.31	F	<7.11	7.25
NGC3400	10h50m45.47s	+28d28m08.7s	1441	24.7	Sa	13.51	12.80	9.81	F	<7.63	<7.19
NGC3412	10h50m53.28s	+13d24m43.7s	860	11.0	S0	11.45	10.72	9.97	F	<6.96	<6.55
NGC3414	10h51m16.24s	+27d58m29.9s	1470	24.5	S0	11.70	10.91	10.69	S	H2	8.28
NGC3457	10h54m48.62s	+17d37m16.2s	1148	20.1	E	13.07	12.36	9.81	F	<7.35	8.07
UGC06062	10h58m37.57s	+09d03m01.6s	2634	38.7	S0	13.78	12.97	10.30	F	<7.93	-
NGC3489	11h00m18.59s	+13d54m04.5s	695	11.7	S0	11.48	10.66	10.20	F	7.2	6.87
NGC3522	11h06m40.46s	+20d05m08.0s	1228	25.5	E	13.47	12.75	9.87	S	<7.28	8.47
UGC06176	11h07m24.68s	+21d39m25.5s	2677	40.1	S0	14.01	13.27	10.09	F	8.58	9.02
IC0676	11h12m39.80s	+09d03m21.0s	1429	24.6	S0	13.36	12.61	9.95	F	8.63	8.27
NGC3599	11h15m26.96s	+18d06m37.4s	839	19.8	S0	12.77	12.06	9.91	F	7.36	<7.03
NGC3605	11h16m46.59s	+18d01m01.8s	661	20.1	E	-	-	-	F	<7.48	<6.83
NGC3607	11h16m54.64s	+18d03m06.3s	942	22.2	S0	-	-	-	F	8.42	<6.92
NGC3608	11h16m58.95s	+18d08m55.3s	1226	22.3	E	-	-	-	S	<7.58	7.16
NGC3626	11h20m03.81s	+18d21m24.6s	1486	19.5	S0	11.80	11.06	10.35	F	8.21	8.94
NGC3630	11h20m16.98s	+02d57m51.8s	1499	25.0	S0	12.67	11.83	10.42	F	<7.6	-
NGC3640	11h21m06.85s	+03d14m05.4s	1298	26.3	E	11.19	10.33	11.10	F	<7.59	-
NGC3641	11h21m08.81s	+03d11m40.5s	1780	25.9	E	14.05	13.20	9.92	F	<7.66	-
NGC3694	11h28m54.13s	+35d24m50.4s	2243	35.2	E	13.74	13.04	10.00	F	<7.91	<7.49
PGC035754	12h58m18.82s	+13d23m29.4s	2534	39.0	S0	14.36	13.62	9.93	F	<7.9	<7.58
IC0719	11h40m18.50s	+09d00m36.0s	1833	29.4	S0	13.52	12.70	10.18	F/S	8.26	8.96
NGC4078	12h04m47.64s	+10d35m44.1s	2546	38.1	S0	13.55	12.74	10.38	F	<7.98	<7.64
NGC4119	12h08m09.62s	+10d22m44.0s	1656	16.5	S0	12.92	12.20	9.72	F	7.88	<7.10
NGC4168	12h12m17.23s	+13d12m19.3s	2286	30.9	E	11.99	11.23	10.71	S	<7.74	<7.46
NGC4179	12h12m52.11s	+01d17m58.9s	1300	16.5	S0	11.86	11.07	10.28	F	<7.28	-
NGC4191	12h13m50.38s	+07d12m03.0s	2646	39.2	S0	13.32	12.55	10.41	S	<7.94	9.19
NGC4215	12h15m54.54s	+06d24m04.1s	2011	31.5	S0	12.71	11.97	10.40	F	<7.83	-

Galaxy	RA J2000.0	Dec J2000.0	cz km/s	D Mpc	Type	g mag	r mag	logM _{star} M_{\odot}	Rot	log M(H ₂) M_{\odot}	log M(HI) M_{\odot}
NGC4233	12h17m07.68s	+07d37m27.8s	2306	33.9	S0	12.68	11.75	10.87	F	<7.89	-
NGC4249	12h17m59.39s	+05d35m54.9s	2618	38.7	S0	14.20	13.45	10.01	F	<7.97	-
NGC4251	12h18m08.25s	+28d10m31.4s	1066	19.1	S0	11.91	11.11	10.41	F	<7.11	<6.97
NGC4255	12h18m56.15s	+04d47m10.1s	1995	31.2	S0	13.12	12.33	10.33	F	<7.78	-
NGC4259	12h19m22.21s	+05d22m35.0s	2497	37.2	S0	14.05	13.28	10.07	S/F	<7.97	-
NGC4261	12h19m23.22s	+05d49m30.8s	2212	30.8	E	11.17	10.32	11.22	S	<7.68	-
NGC4262	12h19m30.58s	+14d52m39.8s	1375	15.4	S0	12.16	11.34	10.17	F	<7.07	8.69
NGC4264	12h19m35.76s	+05d50m48.3s	2518	37.5	S0	13.22	12.46	10.39	F	<7.94	-
NGC4267	12h19m45.24s	+12d47m53.8s	1021	15.8	S0	11.94	11.13	10.25	F	<7.16	<7.17
NGC4268	12h19m47.22s	+05d17m01.1s	2034	31.7	S0	13.21	12.43	10.29	F	<7.83	-
NGC4270	12h19m49.43s	+05d27m48.1s	2331	35.2	S0	12.70	11.95	10.52	F	<7.79	8.37
NGC4278	12h20m06.82s	+29d16m50.7s	620	15.6	E	11.10	10.28	10.60	F	H2	8.80
NGC4283	12h20m20.85s	+29d18m39.4s	1056	15.3	E	12.83	12.04	9.83	F	7.1	<6.36
NGC4281	12h20m21.53s	+05d23m11.1s	2671	24.4	S0	11.84	10.98	10.78	F	<7.88	-
IC0782	12h21m36.97s	+05d45m56.7s	2424	36.3	Sb	13.92	13.23	9.94	F	<7.92	-
NGC4324	12h23m06.17s	+05d15m01.8s	1665	16.5	S0	12.33	11.54	10.10	F	7.69	8.73
NGC4339	12h23m34.95s	+06d04m54.3s	1266	16.0	E	12.10	11.30	10.18	F	<7.15	-
NGC4340	12h23m35.29s	+16d43m20.5s	933	18.4	S0	12.17	11.36	10.30	F	<7.33	<7.03
NGC4342	12h23m39.00s	+07d03m14.4s	761	16.5	S0	12.78	11.97	9.95	F	<7.24	-
NGC4350	12h23m57.87s	+16d41m36.3s	1210	15.4	S0	11.69	10.77	10.56	F	<7.18	<6.88
NGC4365	12h24m28.23s	+07d19m03.1s	1243	23.3	E	10.04	9.24	11.34	S	<7.62	-
NGC4371	12h24m55.43s	+11d42m15.2s	933	17.0	S0	11.41	10.56	10.61	F	<7.29	<7.10
NGC4374	12h25m03.78s	+12d53m13.1s	1017	18.5	E	9.50	8.58	11.59	S	<7.23	<7.26
NGC4377	12h25m12.34s	+14d45m43.8s	1338	17.8	S0	12.47	11.69	10.08	F	<7.26	<7.16
NGC4379	12h25m14.74s	+15d36m26.9s	1074	15.8	S0	12.16	11.41	10.04	F	<7.19	<7.04
NGC4382	12h25m24.11s	+18d11m29.4s	746	17.9	S0	11.07	10.37	10.49	F	<7.39	<6.97
NGC4387	12h25m41.68s	+12d48m37.9s	565	17.9	E	12.81	12.06	9.89	F	<7.39	<7.03
NGC4406	12h26m11.81s	+12d56m45.5s	-224	16.8	E	9.27	8.49	11.31	S	<7.4	8.00
NGC4417	12h26m50.61s	+09d35m03.3s	828	16.0	S0	11.81	11.07	10.17	F	<7.22	-
NGC4425	12h27m13.36s	+12d44m05.3s	1908	16.5	S0	12.52	11.82	9.83	F	<7.2	<6.71
NGC4429	12h27m26.56s	+11d06m27.1s	1104	16.5	S0	11.49	10.61	10.62	F	8.05	7.12
NGC4434	12h27m36.68s	+08d09m15.6s	1070	22.4	E	12.63	11.85	10.22	F	<7.6	-
NGC4435	12h27m40.49s	+13d04m44.2s	791	16.7	S0	11.15	10.35	10.60	F	7.87	<7.23
NGC4442	12h28m03.88s	+09d48m13.4s	547	15.3	S0	11.18	10.35	10.57	F	<7.12	-
NGC4458	12h28m57.57s	+13d14m30.8s	677	16.4	E	12.66	11.92	9.85	S	<7.31	<6.91
NGC4459	12h29m00.01s	+13d58m42.1s	1192	16.1	S0	11.01	10.17	10.70	F	8.24	<6.91
NGC4461	12h29m03.01s	+13d11m01.9s	1924	16.5	S0	11.79	11.00	10.31	F	<7.20	<7.33
NGC4472	12h29m46.80s	+08d00m01.5s	981	17.1	E	10.41	9.54	11.06	S	<7.25	-
NGC4473	12h29m48.88s	+13d25m45.6s	2260	15.3	E	11.11	10.18	10.81	F	<7.07	<6.86
NGC4474	12h29m53.55s	+14d04m06.9s	1611	15.6	S0	12.18	11.35	10.19	F	<7.16	<7.08
NGC4476	12h29m59.08s	+12d20m55.2s	1968	17.6	S0	12.64	11.92	9.88	F	8.05	-
NGC4477	12h30m02.17s	+13d38m11.2s	1338	16.5	S0	11.02	10.22	10.65	F	7.54	<6.95
NGC4478	12h30m17.42s	+12d19m42.8s	1375	17.0	E	12.39	11.59	10.12	F	<7.28	-
NGC4483	12h30m40.65s	+09d00m56.4s	906	16.7	S0	12.86	12.08	9.87	F	<7.2	-
NGC4486	12h30m49.42s	+12d23m28.0s	1284	17.2	E	9.17	8.39	11.37	S	<7.17	-
NGC4489	12h30m52.25s	+16d45m31.9s	961	15.4	E	12.86	12.17	9.62	F	<7.15	<6.74
NGC4486A	12h30m57.71s	+12d16m13.3s	758	18.3	E	12.12	11.55	9.81	F	<0.0	-
NGC4494	12h31m24.10s	+25d46m30.9s	1342	16.6	E	-	-	13.41	F	<7.25	<6.84
NGC4503	12h32m06.19s	+11d10m35.2s	1334	16.5	S0	11.99	11.13	10.38	F	<7.22	<7.14
NGC4526	12h34m03.09s	+07d41m58.3s	617	16.4	S0	10.67	9.79	10.94	F	8.59	-

Galaxy	RA J2000.0	Dec J2000.0	cz km/s	D Mpc	Type	g mag	r mag	logM _{star} M_{\odot}	Rot	log M(H ₂) M_{\odot}	log M(HI) M_{\odot}
NGC4528	12h34m06.07s	+11d19m16.5s	1378	15.8	S0	12.61	11.86	9.86	S/F	<7.15	<7.18
NGC4550	12h35m30.58s	+12d13m15.0s	459	15.5	S0	12.25	11.47	10.05	S	H2	6.89
NGC4551	12h35m37.95s	+12d15m50.3s	1176	16.1	E	12.56	11.79	9.94	F	<7.24	<7.39
NGC4552	12h35m39.88s	+12d33m21.7s	344	15.8	E	10.29	9.49	10.89	S	<7.28	<6.87
NGC4564	12h36m26.98s	+11d26m21.4s	1155	15.8	E	11.71	10.90	10.35	F	<7.25	<6.91
NGC4570	12h36m53.40s	+07d14m47.9s	1787	17.1	S0	11.66	10.86	10.41	F	<7.47	-
NGC4578	12h37m30.56s	+09d33m18.3s	2292	16.3	S0	12.22	11.42	10.15	F	<7.2	-
IC3631	12h39m48.01s	+12d58m26.3s	2822	42.0	S0	13.85	13.41	9.58	F	<7.94	<7.71
NGC4596	12h39m55.94s	+10d10m33.7s	1892	16.5	S0	10.95	10.18	10.60	F	7.31	<7.13
NGC4608	12h41m13.29s	+10d09m20.4s	1850	16.5	S0	11.93	11.14	10.26	F	<7.3	<7.22
NGC4612	12h41m32.75s	+07d18m53.6s	1775	16.6	S0	12.00	11.30	10.05	F	<7.2	-
NGC4621	12h42m02.24s	+11d38m49.3s	467	14.9	E	10.15	9.40	10.80	F	<7.13	<6.86
NGC4623	12h42m10.69s	+07d40m37.0s	1807	17.4	S0	12.79	12.04	9.875	F	<7.21	-
NGC4638	12h42m47.42s	+11d26m33.0s	1152	17.5	S0	11.93	11.16	10.27	F	<7.3	<7.12
NGC4636	12h42m49.87s	+02d41m16.0s	930	14.3	E	10.28	9.52	10.73	S	<6.87	HI
NGC4643	12h43m20.13s	+01d58m42.2s	1333	16.5	S0	11.15	10.30	10.69	F	7.27	HI
NGC4649	12h43m40.01s	+11d33m09.4s	1110	17.3	E	9.39	8.59	11.33	F	<7.44	<7.18
NGC4660	12h44m31.98s	+11d11m25.9s	1087	15.0	E	11.74	10.97	10.21	F	<7.19	<6.88
NGC4624/65	12h45m05.99s	+03d03m20.8s	912	16.5	S0	-	-	-	F	<7.3	-
NGC4694	12h48m15.09s	+10d59m01.0s	1171	16.5	S0	12.08	11.65	9.45	F	8.01	8.21
NGC4710	12h49m38.96s	+15d09m55.8s	1102	16.5	S0	19.09	17.82	10.39	F	8.72	6.84
NGC4733	12h51m06.78s	+10d54m43.5s	925	14.5	E	12.73	12.02	9.66	F	<7.28	<7.12
NGC4754	12h52m17.50s	+11d18m50.0s	1351	16.1	S0	11.38	10.48	10.68	F	<7.18	<7.18
NGC4762	12h52m56.05s	+11d13m50.9s	986	22.6	S0	11.56	10.79	10.64	F	<7.48	<7.40
NGC4803	12h55m33.68s	+08d14m25.5s	2645	39.4	S0	14.28	13.54	9.97	S/F	<7.98	-
PGC044433	15h15m34.61s	+02d14m53.8s	2675	40.1	S0	14.28	13.48	10.11	F	<7.98	<7.66
NGC5574	14h20m55.97s	+03d14m16.8s	1589	23.2	S0	12.68	12.02	9.98	F	<7.51	-
NGC5576	14h21m03.68s	+03d16m15.6s	1506	24.8	E	11.66	10.90	10.66	S	<7.6	-
NGC5611	14h24m04.78s	+33d02m50.6s	1968	24.5	S0	13.20	12.45	10.01	F	<7.57	<7.15
NGC5638	14h29m40.38s	+03d13m59.9s	1652	25.6	E	11.81	10.98	10.77	F	<7.6	-
IC1024	14h31m27.20s	+03d00m32.7s	1479	24.2	S0	13.77	13.10	9.60	F	8.61	HI
UGC09519	14h46m21.09s	+34d22m14.0s	1631	27.6	S0	13.78	12.94	10.06	F	8.77	9.27
NGC5770	14h53m15.02s	+03d57m35.0s	1471	18.5	S0	12.75	12.01	9.92	F	<7.34	-
NGC5813	15h01m11.23s	+01d42m07.1s	1956	31.3	E	11.82	10.94	11.04	S	<7.69	-
NGC5831	15h04m07.00s	+01d13m11.7s	1645	26.4	E	12.54	11.73	10.46	S	<7.85	-
NGC5838	15h05m26.26s	+02d05m57.6s	1341	21.8	S0	11.56	10.69	10.81	F	<7.56	-
NGC5839	15h05m27.49s	+01d38m05.3s	1220	22.0	S0	13.04	12.22	10.12	F	<7.38	-
NGC5845	15h06m00.81s	+01d38m01.7s	1472	25.2	E	13.09	12.22	10.32	F	<7.5	-
NGC5846	15h06m29.28s	+01d36m20.2s	1712	24.2	E	-	-	0.0	S	<7.78	-
NGC5854	15h07m47.70s	+02d34m07.1s	1663	26.2	S0	12.59	11.89	10.21	F	<7.6	HI
NGC5864	15h09m33.56s	+03d03m09.9s	1874	29.0	S0	12.56	11.80	10.43	F	<7.74	-
NGC5869	15h09m49.44s	+00d28m12.1s	2065	24.9	S0	12.59	11.69	10.57	F	<7.63	-
PGC054452	16h02m11.63s	+07d05m10.0s	1918	29.5	S0	14.14	13.42	9.732	F	<7.73	-
NGC6010	15h54m19.15s	+00d32m35.0s	2022	30.6	S0	13.01	12.11	10.59	F	<7.78	HI
NGC6014	15h55m57.40s	+05d55m54.8s	2381	35.8	S0	13.44	12.67	10.28	F	8.77	HI
NGC6017	15h57m15.44s	+05d59m54.2s	1788	29.0	E	13.53	12.72	10.15	F	<7.73	HI
PGC056772	16h02m11.63s	+07d05m09.9s	2655	39.5	S0	14.37	13.57	10.06	F	8.19	-

Table 3. General parameters of the 147 sampled galaxies

Galaxy	RA J2000.0	Dec J2000.0	cz km/s	D Mpc	Type	<i>g</i> mag	<i>r</i> mag	logM _{star} M _⊙
NGC2480	07h57m10.44s	+23d46m47.3s	2345	34.6	ScB	14.36	13.83	9.39
NGC2779	09h12m28.29s	+35d03m13.5s	2105	31.8	-	14.52	13.80	9.64
NGC5636	14h29m39.02s	+03d15m58.7s	1745	26.9	SABr	13.84	13.05	8.18
J125830	12h58m30.84s	+26d59m41.8s	7453	103.0	-	17.80	17.65	8.91
J125838	12h58m38.69s	+27d00m47.5s	7015	97.0	-	17.44	16.98	8.71
J125853	12h58m53.79s	+27d23m19.1s	7654	105.0	-	17.95	17.52	8.60
J125916	12h59m17.14s	+27d06m06.7s	-	-	Src	22.27	21.03	7.84
J130045	13h00m45.04s	+28d31m42.5s	-	-	-	19.09	18.84	7.70
J130254	13h02m54.19s	+28d30m15.9s	8274	113.0	-	18.54	18.52	9.91
J162054	16h20m54.48s	+39d54m30.3s	8627	115.0	-	16.58	16.23	9.18
J162431	16h24m31.41s	+40d41m04.0s	8820	117.0	-	17.06	16.87	8.67
J162447	16h24m47.57s	+39d44m05.1s	8947	119.0	SB	15.61	15.09	9.94
J162549	16h25m49.26s	+40d20m42.7s	8637	115.0	Irr	14.74	14.39	9.91
J162715	16h27m14.09s	+38d57m01.0s	-	-	Src	22.35	21.29	8.20
J162820	16h28m20.11s	+40d55m59.8s	8762	116.0	-	15.95	15.46	9.72
J162828	16h28m28.62s	+40d43m14.8s	8616	114.0	-	16.05	15.47	9.85
J162915	16h29m15.12s	+40d14m27.4s	8901	118.0	S	16.38	15.84	9.67
J162916	16h29m16.16s	+40d15m36.6s	8477	113.0	Sbc	16.51	16.15	9.21
J163037	16h30m38.04s	+40d42m30.8s	7979	106.0	S	15.97	15.68	9.23
J163158	16h31m58.55s	+39d56m52.2s	8472	112.0	-	17.08	16.74	8.93

Table 4. General parameters of the 20 filler targets

Galaxy	ref H α	Am _{ON} 2015	Am _{OFF} 2015	Am _{ON} 2016	Am _{OFF} 2016	Tex _{ON} 2015	Tex _{OFF} 2015	Tex _{ON} 2016	Tex _{OFF} 2016
UGC03960	1	1.01	1.00	-	-	300	60	-	-
NGC2481	1	1.00	1.00	-	-	300	60	-	-
NGC2577	1	1.02	1.03	-	-	300	60	-	-
NGC2592	1	1.03	1.03	-	-	300	60	-	-
NGC2594	1	1.01	1.01	-	-	300	60	-	-
NGC2679	1	1.00	1.00	-	-	300	60	-	-
NGC2764	1	1.03	1.03	-	-	300	60	-	-
NGC2778	1	1.00	1.01	-	-	300	60	-	-
NGC2859	1	1.01	1.01	-	-	300	60	-	-
NGC2962	1	1.21	1.22	-	-	300	60	-	-
NGC3032	1	1.01	1.01	-	-	300	60	-	-
PGC028887	1	1.14	1.15	-	-	300	60	-	-
NGC3098	1	1.04	1.05	-	-	300	60	-	-
PGC029321	1	1.07	1.07	1.06	1.07	300	60	300	60
NGC3156	1	1.14	1.17	1.15	1.15	300	60	300	60
NGC3193	1	1.04	1.04	-	-	300	60	-	-
NGC3226	3	-	-	-	-	-	-	-	-
NGC3230	1	1.08	1.08	-	-	300	60	-	-
NGC3245	1	1.00	1.00	1.03	1.03	300	60	300	60
NGC3248	1	1.02	1.02	-	-	300	60	-	-
NGC3301	1	1.03	1.03	1.05	1.05	300	60	300	60
NGC3377	1	1.05	1.05	1.08	1.08	300	60	300	60
NGC3379	1	1.07	1.08	-	-	300	60	-	-
NGC3384	1	1.07	1.07	-	-	300	60	-	-
NGC3400	1	1.00	1.01	1.03	1.03	300	60	300	60
NGC3412	1	-	-	1.08	1.08	-	-	300	60
NGC3414	2	-	-	-	-	-	-	-	-
NGC3457	3	-	-	-	-	-	-	-	-
UGC06062	1	1.08	1.08	-	-	300	60	-	-
NGC3489	10	-	-	-	-	-	-	-	-
NGC3522	1	1.03	1.03	-	-	300	60	-	-
UGC06176	1	1.02	1.02	1.06	1.06	300	60	300	60
IC0676	1	1.08	1.08	-	-	300	60	-	-
NGC3599	1	1.02	1.02	-	-	300	60	-	-
NGC3605	1	1.02	1.02	1.07	1.07	300	60	300	60
NGC3607	1	1.02	1.02	1.07	1.07	300	60	300	60
NGC3608	1	-	-	1.05	1.06	-	-	300	60
NGC3626	1	1.02	1.02	1.07	1.07	300	60	300	60
NGC3630	1	-	-	1.15	1.15	-	-	300	60
NGC3640	1	1.14	1.14	1.52	1.51	300	60	300	60
NGC3641	1	1.14	1.14	1.52	1.51	300	60	300	60
NGC3694	1	1.00	1.00	-	-	300	60	-	-
PGC035754	1	-	-	1.04	1.04	-	-	300	60
IC0719	1	1.08	1.08	1.12	1.12	300	60	300	60
NGC4078	1	-	-	1.12	1.12	-	-	300	60
NGC4119	1	1.07	1.07	1.10	1.1	300	60	300	60
NGC4168	9	-	-	-	-	-	-	-	-
NGC4179	1	1.18	1.19	1.25	1.25	300	60	300	60
NGC4191	10	-	-	-	-	-	-	-	-
NGC4215	1	-	-	1.16	1.17	-	-	300	60

Galaxy	ref H α	Am _{ON} 2015	Am _{OFF} 2015	Am _{ON} 2016	Am _{OFF} 2016	Tex _{ON} 2015	Tex _{OFF} 2015	Tex _{ON} 2016	Tex _{OFF} 2016
NGC4233	1	1.09	1.10	1.13	1.13	300	60	300	60
NGC4249	1	-	-	1.14	1.14	-	-	300	60
NGC4251	1	1.05	1.05	-	-	300	60	-	-
NGC4255	1	-	-	1.14	1.14	-	-	300	60
NGC4259	1	-	-	1.11	1.11	-	-	300	60
NGC4261	1	1.10	1.10	1.15	1.15	300	60	360	60
NGC4262	10	-	-	-	-	-	-	-	-
NGC4264	1	1.10	1.10	1.15	1.15	300	60	300	60
NGC4267	1	-	-	1.05	1.05	-	-	300	60
NGC4268	9	-	-	-	-	-	-	-	-
NGC4270	10	-	-	-	-	-	-	-	-
NGC4278	1	1.00	1.00	1.02	1.02	300	60	300	60
NGC4283	1	1.00	1.00	-	-	300	60	-	-
NGC4281	9	-	-	-	-	-	-	-	-
IC0782	1	1.14	1.15	-	-	300	60	-	-
NGC4324	9	-	-	-	-	-	-	-	-
NGC4339	1	1.10	1.10	-	-	300	60	-	-
NGC4340	1	1.04	1.04	-	-	300	60	-	-
NGC4342	1	-	-	1.09	1.09	-	-	300	60
NGC4350	1	1.03	1.03	1.07	1.07	300	60	300	60
NGC4365	8	-	-	-	-	-	-	-	-
NGC4371	1	1.06	1.06	-	-	300	60	-	-
NGC4374	10	-	-	-	-	-	-	-	-
NGC4377	1	1.04	1.04	-	-	300	60	-	-
NGC4379	1	1.05	1.05	1.12	1.12	300	60	300	60
NGC4382	1	-	-	1.03	1.03	-	-	300	60
NGC4387	1	-	-	1.07	1.07	-	-	300	60
NGC4406	10	-	-	-	-	-	-	-	-
NGC4417	1	-	-	1.10	1.10	-	-	300	60
NGC4425	9	-	-	-	-	-	-	-	-
NGC4429	9	-	-	-	-	-	-	-	-
NGC4434	1	1.08	1.08	-	-	300	60	-	-
NGC4435	1	1.07	1.06	1.08	1.08	300	60	300	60
NGC4442	1	-	-	1.10	1.10	-	-	300	60
NGC4458	1	-	-	1.09	1.09	-	-	300	60
NGC4459	1	-	-	1.06	1.06	-	-	300	60
NGC4461	7	-	-	-	-	-	-	-	-
NGC4472	10	-	-	-	-	-	-	-	-
NGC4473	7	-	-	-	-	-	-	-	-
NGC4474	1	1.05	1.05	-	-	300	60	-	-
NGC4476	1	-	-	1.10	1.10	-	-	300	60
NGC4477	2	-	-	-	-	-	-	-	-
NGC4478	1	-	-	1.11	1.10	-	-	300	60
NGC4483	1	1.12	1.11	1.23	1.22	300	60	300	60
NGC4486	10	-	-	-	-	-	-	-	-
NGC4489	1	-	-	1.09	1.09	-	-	300	60
NGC4486A	1	-	-	1.14	1.13	-	-	300	60
NGC4494	1	1.23	1.21	-	-	300	60	-	-
NGC4503	9	-	-	-	-	-	-	-	-
NGC4526	1	-	-	1.09	1.09	-	-	300	60

Galaxy	ref H α	Am _{ON} 2015	Am _{OFF} 2015	Am _{ON} 2016	Am _{OFF} 2016	Tex _{ON} 2015	Tex _{OFF} 2015	Tex _{ON} 2016	Tex _{OFF} 2016
NGC4528	1	-	-	1.18	1.17	-	-	300	60
NGC4550	1	1.09	1.09	1.09	1.09	300	60	300	60
NGC4551	1	1.09	1.09	1.09	1.09	300	60	300	60
NGC4552	11	-	-	-	-	-	-	-	-
NGC4564	1	1.08	1.07	-	-	300	60	-	-
NGC4570	1	1.14	1.13	-	-	300	60	-	-
NGC4578	1	-	-	1.20	1.20	-	-	300	60
IC3631	1	1.08	1.07	-	-	300	60	-	-
NGC4596	7	-	-	-	-	-	-	-	-
NGC4608	1	1.13	1.13	1.22	1.21	300	60	300	60
NGC4612	1	-	-	1.30	1.29	-	-	300	60
NGC4621	1	1.14	1.13	-	-	300	60	-	-
NGC4623	1	-	-	1.24	1.23	-	-	300	60
NGC4638	1	1.15	1.14	-	-	300	60	-	-
NGC4636	7	-	-	-	-	-	-	-	-
NGC4643	8	-	-	-	-	-	-	-	-
NGC4649	11	-	-	-	-	-	-	-	-
NGC4660	1	1.12	1.11	1.19	1.19	300	60	300	60
NGC4624/65	1	1.19	1.18	-	-	300	60	-	-
NGC4694	9	-	-	-	-	-	-	-	-
NGC4710	6	-	-	-	-	-	-	-	-
NGC4733	1	1.17	1.16	1.18	1.18	300	60	300	60
NGC4754	1	1.17	1.16	-	-	300	60	-	-
NGC4762	1	1.16	1.16	1.2	1.19	300	60	300	60
NGC4803	1	1.20	1.2	-	-	300	60	-	-
PGC044433	1	1.05	1.05	1.17	1.16	300	60	300	60
NGC5574	1	1.13	1.14	1.16	1.16	300	60	300	60
NGC5576	1	1.13	1.14	1.16	1.16	300	60	300	60
NGC5611	1	1.00	1.01	1.04	1.03	300	60	300	60
NGC5638	1	1.14	1.14	-	-	300	60	-	-
IC1024	1	1.14	1.14	1.14	1.14	300	60	300	60
UGC09519	1	1.01	1.01	1.03	1.03	300	60	300	60
NGC5770	1	1.12	1.12	1.13	1.13	300	60	300	60
NGC5813	1	1.15	1.15	-	-	300	60	-	-
NGC5831	1	1.15	1.15	1.19	1.18	300	60	300	60
NGC5838	1	1.16	1.16	-	-	300	60	-	-
NGC5839	1	1.15	1.15	1.16	1.16	300	60	300	60
NGC5845	1	1.18	1.18	1.22	1.21	300	60	300	60
NGC5846	1	1.15	1.15	1.17	1.17	300	60	300	60
NGC5854	1	1.16	1.16	1.22	1.22	300	60	300	60
NGC5864	1	1.16	1.15	1.17	1.17	300	60	300	60
NGC5869	1	1.21	1.20	-	-	300	60	-	-
PGC054452	1	1.19	1.19	1.26	1.26	300	60	300	60
NGC6010	1	1.17	1.17	1.16	1.16	300	60	300	60
NGC6014	1	1.11	1.11	1.16	1.15	300	60	300	60
NGC6017	1	1.12	1.12	-	-	300	60	-	-
PGC056772	1	1.11	1.11	1.16	1.15	300	60	300	60

Table 5. H α observational parameters of the 147 observed galaxies

Galaxy	Ref	Am _{ON} 2015	Am _{OFF} 2015	Am _{ON} 2016	Am _{OFF} 2016	Tex _{ON} 2015	Tex _{POFF} 2015	Tex _{ON} 2016	Tex _{POFF} 2016
NGC2480	1	1.00	1.00	-	-	300	60	-	-
NGC2779	1	1.00	1.01	-	-	300	60	-	-
NGC5636	1	1.14	1.14	-	-	300	60	-	-
J125830	1	-	-	1.03	1.02	-	-	600	120
J125838	1	-	-	1.10	1.09	-	-	600	120
J125853	1	-	-	1.19	1.17	-	-	600	120
J125916	1	-	-	1.13	1.12	-	-	600	120
J130045	1	-	-	1.24	1.22	-	-	600	120
J130254	1	-	-	1.02	1.01	-	-	600	120
J162054	1	-	-	1.01	1.01	-	-	420	60
J162431	1	-	-	1.03	1.03	-	-	420	120
J162447	1	-	-	1.01	1.01	-	-	420	60
J162549	1	-	-	1.01	1.01	-	-	420	60
J162715	1	-	-	1.01	1.01	-	-	420	60
J162820	1	-	-	1.03	1.02	-	-	420	60
J162828	1	-	-	1.03	1.02	-	-	600	120
J162915	1	-	-	1.01	1.01	-	-	600	120
J162916	1	-	-	1.01	1.01	-	-	600	120
J163037	1	-	-	1.03	1.02	-	-	600	120
J163158	1	-	-	1.04	1.04	-	-	420	60

Table 6. H α observational parameters of the 20 filler targets

Galaxy	$EW_{3''}$ Å	\pm Å	$LogF_{3''}$ erg cm ⁻² s ⁻¹	\pm erg cm ⁻² s ⁻¹	EW_{Tot} Å	\pm Å	$LogF_{Tot}$ erg cm ⁻² s ⁻¹	\pm erg cm ⁻² s ⁻¹	log SFR $M_{\odot}yr^{-1}$	Spec	Spec Ty	det	morf H α	HST	ref H α
UGC03960	-2.47	3.07	-14.60	0.35	-3.89	3.76	-13.38	0.29	-2.15	SDSS	PAS	2	c	0	1
NGC2481	-0.43	2.98	<-14.79	0.89	3.66	2.99	-	-	-	LOI	RET	3	-	0	1
NGC2577	-6.29	3.02	-13.72	0.16	1.71	3.07	-	-	-	LOI	PAS	3	-	-	1
NGC2592	2.32	2.93	-	-	4.82	3.27	-	-	-	LOI	PAS	3	-	0	1
NGC2594	-1.14	3.01	-14.43	0.56	2.93	2.99	-	-	-	LOI	PAS	3	-	-	1
NGC2679	-0.28	2.98	<-15.26	1.05	1.41	4.16	-	-	-	SDSS	PAS	3	-	-	1
NGC2764	-81.01	4.69	-13.37	0.01	-17.25	3.74	-12.61	0.08	-1.23	LOI	HII	1	d	-	1
NGC2778	-6.53	3.02	-13.70	0.16	-1.13	3.15	-13.48	0.57	-2.60	LOI	PAS	2	c	0	1
NGC2859	-5.65	2.94	-13.47	0.18	-2.02	4.59	-12.59	0.51	-1.54	HO	AGN	2	c	0	1
NGC2962	-7.12	3.01	-13.69	0.15	-3.00	3.60	-12.78	0.34	-1.53	LOI	RET	2	D	1	1
NGC3032	-14.44	3.01	-12.76	0.08	-20.97	3.23	-11.78	0.06	-0.93	LOI	HII	1	d	1	1
PGC028887	-1.30	3.03	-14.70	0.52	-3.65	3.41	-13.47	0.28	-2.06	SDSS	PAS	2	c	0	1
NGC3098	-1.89	2.88	-14.18	0.40	-0.82	2.90	<-13.45	0.65	<-2.54	LOI	PAS	3	-	-	1
PGC029321	-75.41	1.61	-13.56	0.02	-35.94	1.42	-13.04	0.04	-1.63	SDSS	AGN	1	D	-	1
NGC3156	1.70	1.37	-	-	3.46	2.06	-	-	-	SDSS	AGN	3	-	1	1
NGC3193	-0.99	2.86	<-14.19	0.58	0.40	3.67	-	-	-	HO	PAS	3	-	0	1
NGC3226	-19.00	-	-	-	-8.00	-	-12.82	-	-1.92	NED	SEY	1	d	1	3
NGC3230	-2.15	3.01	-14.16	0.37	2.23	3.00	-	-	-	NEDMH	PAS	3	-	-	1
NGC3245	-5.90	1.29	-13.40	0.17	-1.90	1.31	-12.72	0.40	-1.92	NED	AGN	2	d	0	1
NGC3248	-2.80	2.90	-14.06	0.30	-0.47	3.06	<-13.80	0.87	<-2.83	LOI	PAS	3	-	-	1
NGC3301	-4.95	1.3	-13.56	0.20	-0.74	1.49	<-13.32	0.74	<-2.42	NED	AGN	3	D	-	1
NGC3377	8.00	1.34	-	-	1.73	2.37	-	-	-	NED	PAS	3	-	0	1
NGC3379	-2.84	2.93	-13.46	0.30	-0.83	3.12	<-12.40	0.67	<-2.19	HO	AGN	3	-	1	1
NGC3384	1.70	3.01	-	-	0.33	3.33	-	-	-	HO	PAS	3	-	0	1
NGC3400	6.67	1.31	-	-	1.97	1.39	-	-	-	SDSS	PAS	3	-	-	1
NGC3412	7.41	2.88	-	-	-0.61	2.99	<-13.05	1.05	<-2.78	HO	PAS	3	-	0	1
NGC3414	-	-	-	-	-1.00	-	-12.89	-	-1.93	NED	AGN	2	-	0	2
NGC3457	-	-	-	-	2.0	3.0	-	-	-	LOI	PAS	3	-	-	3
UGC06062	7.47	2.97	<-15.00	-	3.38	3.15	-	-	-	SDSS	PAS	3	-	0	1
NGC3489	-19.00	-	-	-	-1.00	-	-12.13	-	-1.81	NED	RET	2	-	1	8
NGC3522	-3.89	2.90	-14.05	0.24	-4.44	3.00	-13.04	0.22	-2.04	SDSS	AGN	2	c	0	1
UGC06176	-59.75	1.72	-13.16	0.02	-8.92	1.57	-13.04	0.14	-1.65	SDSS	HII	1	d	1	1
IC0676	-57.35	3.84	-13.27	0.02	-11.82	3.27	-12.50	0.10	-1.53	SDSS	HII	1	d	1	1
NGC3599	-9.15	3.04	-13.56	0.12	-7.95	3.97	-12.48	0.17	-1.70	LOI	AGN	1	c	1	1
NGC3605	2.56	1.38	-	-	-2.42	2.05	<-13.33	0.46	<-2.54	LOI	PAS	3	-	0	1
NGC3607	-2.73	1.28	-13.82	0.32	-4.00	1.76	-12.13	0.3	-1.25	NED	AGN	2	d	1	1
NGC3608	2.19	2.83	-	-	-0.42	3.00	<-13.37	1.20	<-2.49	HO	AGN	3	-	0	1
NGC3626	2.59	1.27	-	-	-4.38	1.36	-12.40	0.23	-1.63	NED	AGN	2	d	0	1
NGC3630	3.84	2.84	-	-	1.97	6.40	-	-	-	LOI	PAS	3	-	0	1
NGC3640	2.17	1.28	-	-	-1.11	1.77	<-12.79	0.66	<-1.76	NED	PAS	3	-	0	1
NGC3641	1.41	1.33	-	-	9.27	1.79	-	-	-	LOI	PAS	3	-	-	1
NGC3694	-25.36	3.31	-13.43	0.05	-12.45	3.24	-12.71	0.09	-1.43	SDSS	HII	1	c	1	1
PGC035754	0.95	3.01	-	-	0.37	3.46	-	-	-	SDSS	PAS	3	-	-	1
IC0719	-5.21	1.45	-14.28	0.21	-16.27	1.40	-12.57	0.07	-1.45	SDSS	AGN	1	d	-	1
NGC4078	-5.66	3.06	-13.92	0.31	0.98	3.07	-	-	-	LOI	PAS	3	-	-	1
NGC4119	-7.91	1.49	-14.18	0.15	-7.84	1.55	-12.28	0.15	-1.66	SDSS	HII	1	d	-	1
NGC4168	-7.00	-	-	-	-5.00	-	-12.84	-	-1.67	NED	RET	1	-	0	7
NGC4179	2.89	1.27	-	-	-0.21	1.29	<-13.68	1.16	<-3.06	NED	PAS	3	-	0	1
NGC4191	-4.00	-	-	-	-2.90	-	-13.13	-	-1.76	SDSS	RET	2	-	1	8
NGC4215	8.22	2.89	-	-	9.64	2.89	-	-	-	LOI	PAS	3	-	-	1

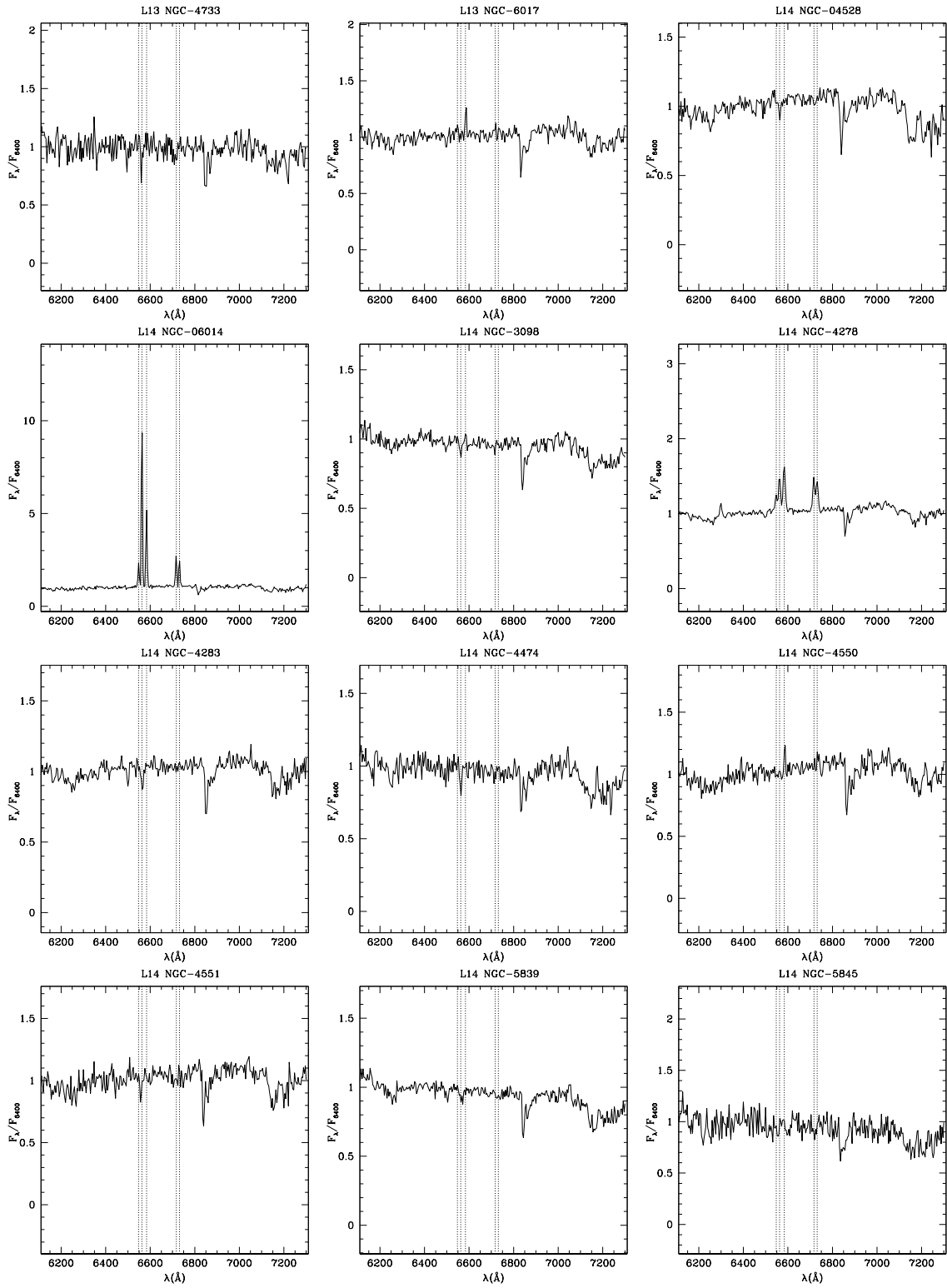
Galaxy	$EW_{3''}$ Å	\pm Å	$LogF_{3''}$ erg cm ⁻² s ⁻¹	\pm erg cm ⁻² s ⁻¹	EW_{Tot} Å	\pm Å	$LogF_{Tot}$ erg cm ⁻² s ⁻¹	\pm erg cm ⁻² s ⁻¹	log SFR $M_{\odot}yr^{-1}$	Spec	Spec Ty	det	morf H α	HST	ref H α
NGC4233	-0.40	1.38	-15.02	0.94	-1.14	1.53	-13.32	0.60	-2.07	SDSS	AGN	2	c	1	1
NGC4249	-1.80	3.08	-14.81	0.64	4.16	3.57	-	-	-	SDSS	PAS	3	-	-	1
NGC4251	7.05	2.82	-	-	-2.02	2.97	<-12.52	0.39	<-1.77	HO	PAS	3	-	-	1
NGC4255	7.45	2.90	-	-	4.74	2.92	-	-	-	NEDMH	PAS	3	-	0	1
NGC4259	-1.74	3.04	-14.59	0.66	1.95	3.16	-	-	-	SDSS	PAS	3	-	-	1
NGC4261	-10.03	1.64	-13.36	0.11	-2.66	2.11	-12.39	0.39	-1.23	NED	AGN	2	c	1	1
NGC4262	4.00	-	-	-	-3.40	-	<-12.62	-	<-2.06	NED	PAS	3	-	0	8
NGC4264	1.60	1.69	-	-	0.30	1.91	-	-	-	SDSS	PAS	3	-	-	1
NGC4267	7.25	2.82	-	-	0.52	3.29	-	-	-	HO	PAS	3	-	0	1
NGC4268	0.00	-	-	-	-2.00	-	<-13.23	-	<-2.04	SDSS	PAS	3	-	-	7
NGC4270	1.00	-	-	-	-2.10	-	<-12.83	-	<-1.55	LOI	PAS	3	-	0	8
NGC4278	-16.23	1.46	-12.90	0.07	-4.01	2.21	-12.21	0.35	-1.64	LOI	AGN	2	c	1	1
NGC4283	-2.72	2.90	-14.00	0.31	-1.28	3.22	-13.29	0.54	-2.73	LOI	PAS	2	c	0	1
NGC4281	0.00	-	-	-	-4.00	-	<-12.41	-	<-1.45	NED	RET	3	-	1	7
IC0782	0.43	3.08	-	-	2.41	3.74	-	-	-	SDSS	PAS	3	-	-	1
NGC4324	-1.00	-	-	-	-6.00	-	-12.40	-	-1.78	NED	RET	1	-	-	7
NGC4339	-0.23	2.86	<-15.12	1.12	-0.23	3.55	<-13.85	1.21	<-3.26	HO	PAS	3	-	0	1
NGC4340	-2.06	2.93	-14.09	0.38	0.98	3.47	-	-	-	HO	PAS	3	-	0	1
NGC4342	11.37	2.92	-	-	4.57	2.97	-	-	-	NED	PAS	3	-	0	1
NGC4350	2.55	1.27	-	-	-0.13	1.41	<-13.85	1.38	<-3.29	NED	AGN	3	-	0	1
NGC4365	-	-	-	-	-2.0	3.0	-	-	-	HO	PAS	3	-	0	8
NGC4371	-2.04	2.93	-14.10	0.38	-2.04	3.64	-12.53	0.44	-1.88	HO	PAS	2	D	1	1
NGC4374	-	-	-	-	-1.00	-	-12.42	-	-1.70	NED	AGN	2	-	1	8
NGC4377	-2.79	2.87	-13.75	0.30	-1.44	2.94	-13.06	0.48	-2.37	LOI	PAS	2	-	0	1
NGC4379	3.72	1.30	-	-	0.90	1.50	-	-	-	NED	PAS	3	-	0	1
NGC4382	9.22	2.94	-	-	-2.98	4.02	<-11.91	0.58	<-1.22	HO	PAS	3	-	0	1
NGC4387	1.13	3.24	-	-	1.03	3.33	-	-	-	SDSS	PAS	3	-	0	1
NGC4406	-	-	-	-	-13.00	-	-12.02	-	-1.38	NED	PAS	1	F	0	9,11
NGC4417	5.05	2.92	-	-	0.69	3.08	-	-	-	HO	PAS	3	-	0	1
NGC4425	0.00	-	-	-	-1.00	-	<-13.17	-	<-2.55	SDSS	PAS	3	-	0	7
NGC4429	-4.00	-	-	-	-5.00	3.00	-13.15	0.13	-2.53	NED	RET	1	-	1	7
NGC4434	-2.19	2.89	-14.07	0.36	0.38	2.96	-	-	-	LOI	PAS	3	-	0	1
NGC4435	-2.63	1.35	-13.87	0.33	-0.32	1.38	-13.41	1.02	-2.78	NED	AGN	2	c	1	1
NGC4442	8.23	3.19	-	-	1.68	3.37	-	-	-	HO	PAS	3	-	0	1
NGC4458	5.18	3.06	-	-	6.64	3.40	-	-	-	LOI	PAS	3	-	0	1
NGC4459	-6.26	2.90	-13.86	0.25	-2.88	3.83	-12.89	0.51	-2.29	NED	LIN	2	c	1	1
NGC4461	-	-	-	-	1.0	1.0	-	-	-	HO	PAS	3	-	0	7
NGC4472	-	-	-	-	-1.00	-	<-12.76	-	<-2.11	NED	PAS	3	-	0	8
NGC4473	-	-	-	-	-0.60	-	<-13.58	-	<-3.02	NED	PAS	3	-	0	5
NGC4474	1.07	2.88	-	-	1.76	3.02	-	-	-	LOI	PAS	3	-	0	1
NGC4476	-6.40	3.5	-14.80	0.5	-3.87	3.38	-13.52	0.46	-2.84	SDSS	LIN	2	d	1	1
NGC4477	-	-	-	-	-	-	<-12.90	0.13	<-2.28	HO	SEY	3	-	1	2
NGC4478	5.93	2.82	-	-	-2.00	2.98	<-12.87	0.61	<-2.22	HO	PAS	3	-	0	1
NGC4483	0.10	1.36	-	-	-0.69	1.56	-13.71	0.78	-3.08	SDSS	PAS	3	-	0	1
NGC4486	-38.00	-	-	-	-2.00	-	-11.93	-	-1.27	NED	AGN	2	F	1	10
NGC4489	-2.11	2.94	-14.44	0.58	-3.79	3.35	-12.99	0.45	-2.43	SDSS	PAS	2	-	0	1
NGC4486A	-	-	-	-	-	-	-	-	-	-	-	3	-	0	1
NGC4494	-3.04	2.88	-13.65	0.28	-5.26	3.47	-11.99	0.21	-1.36	HO	RET	1	D	0	1
NGC4503	0.0	-	-	-	-2.00	-	<-12.52	-	<-1.90	NED	PAS	3	-	0	7
NGC4526	-6.37	3.53	-13.55	0.33	-3.89	3.95	-12.54	0.80	-2.23	NED	AGN	2	d	1	1

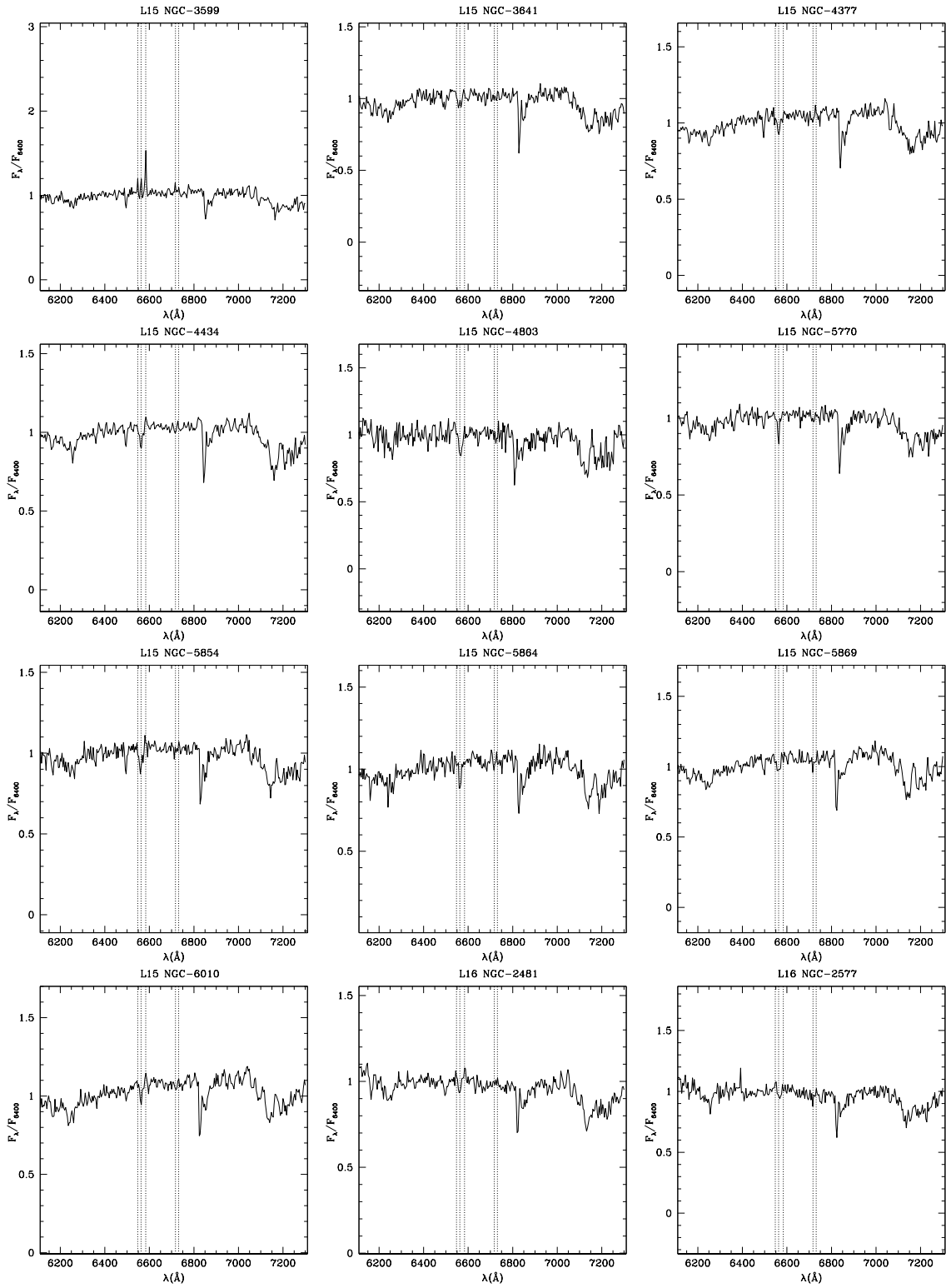
Galaxy	$EW_{3''}$ Å	± Å	$LogF_{3''}$ erg cm ⁻² s ⁻¹	± erg cm ⁻² s ⁻¹	EW_{Tot} Å	± Å	$LogF_{Tot}$ erg cm ⁻² s ⁻¹	± erg cm ⁻² s ⁻¹	log SFR $M_{\odot}yr^{-1}$	Spec	Spec Ty	det	morf H α	HST	ref H α
NGC4528	-4.85	2.90	-13.82	0.34	0.82	2.92	-	-	-	LOI	PAS	3	-	0	1
NGC4550	-4.78	1.61	-13.93	0.24	-5.74	1.66	-12.48	0.21	-1.91	LOI	AGN	1	d	1	1
NGC4551	-1.19	1.33	-14.61	0.54	-1.64	1.42	-13.18	0.47	-2.58	LOI	PAS	2	d	0	1
NGC4552	-	-	-	-	-1.00	-	<-13.01	-	<-2.43	NED	RET	3	-	0	9
NGC4564	0.28	2.85	-	-	1.15	3.02	-	-	-	HO	PAS	3	-	0	1
NGC4570	-0.61	2.91	<-14.26	0.75	-0.35	2.95	<-13.31	0.97	<-2.66	HO	PAS	3	-	0	1
NGC4578	-4.54	3.04	-13.92	0.37	-0.99	3.67	<-13.18	0.94	<-2.57	HO	PAS	3	-	0	1
IC3631	2.88	3.02	-	-	2.09	3.15	-	-	-	SDSS	PSB	3	-	-	1
NGC4596	-	-	-	-	1.0	1.0	-	-	-	HO	RET	3	-	0	7
NGC4608	1.54	1.33	-	-	-0.98	1.77	<-13.04	0.70	<-2.42	NED	PAS	3	-	-	1
NGC4612	3.02	2.88	-	-	1.75	2.90	-	-	-	HO	PAS	3	-	0	1
NGC4621	0.73	3.41	-	-	-1.26	3.96	<-12.43	0.61	<-1.90	HO	PAS	3	-	0	1
NGC4623	-3.35	2.98	-14.40	0.45	3.28	2.91	-	-	-	LOI	PAS	3	-	0	1
NGC4638	-3.06	2.88	-13.82	0.28	-1.44	2.93	-12.99	0.48	-2.32	HO	PAS	2	d	1	1
NGC4636	-	-	-	-	-0.70	-	<-12.67	-	<-2.17	NED	AGN	3	-	0	5
NGC4643	-	-	-	-	-1.90	-	-12.30	-	-1.68	NED	RET	2	-	-	6
NGC4649	0.00	-	-	-	-1.00	-	<-12.56	-	<-1.90	NED	PAS	3	-	0	9
NGC4660	3.65	1.26	-	-	1.58	1.42	-	-	-	NED	PAS	3	-	0	1
NGC4624/65	2.29	2.90	-	-	3.58	3.55	-	-	-	NED	PAS	3	-	-	1
NGC4694	-28.00	-	-	-	-6.00	-	-12.87	-	-2.25	NED	HII	1	F	1	7
NGC4710	-	-	-	-	-19.00	-	-11.39	-	-0.77	NED	HII	1	-	1	4
NGC4733	4.48	1.47	-	-	3.59	1.52	-	-	-	LOI	PAS	3	-	0	1
NGC4754	0.86	2.85	-	-	-1.95	3.37	<-12.46	0.43	<-1.86	HO	PAS	3	-	0	1
NGC4762	6.53	1.50	-	-	0.17	2.29	-	-	-	NED	AGN	3	-	0	1
NGC4803	0.39	3.07	-	-	1.29	3.03	-	-	-	NEDMH	PAS	3	-	-	1
PGC044433	7.11	1.35	-	-	5.65	1.36	-	-	-	SDSS	PAS	3	-	-	1
NGC5574	2.45	1.35	-	-	3.03	2.37	-	-	-	SDSS	PAS	3	-	0	1
NGC5576	5.46	1.22	-	-	0.69	2.52	-	-	-	NED	PAS	3	-	0	1
NGC5611	-4.51	1.39	-13.86	0.22	-1.28	1.63	-13.57	0.58	-2.61	NEDMH	PAS	2	c	-	1
NGC5638	-0.15	2.90	<-15.29	1.29	0.63	2.96	-	-	-	HO	PAS	3	-	0	1
IC1024	-82.04	2.13	-13.50	0.02	-34.60	1.62	-12.33	0.04	-1.38	NEDMH	HII	1	d	1	1
UGC09519	-3.76	1.36	-14.14	0.25	-3.94	1.38	-13.34	0.25	-2.27	SDSS	AGN	2	d	-	1
NGC5770	3.50	1.29	-	-	0.99	1.51	-	-	-	LOI	PAS	3	-	-	1
NGC5813	-1.24	2.95	-14.23	0.52	-0.92	4.06	-	-	-	HO	AGN	3	-	1	1
NGC5831	-3.07	1.33	-13.98	0.29	-4.42	1.71	-12.65	0.27	-1.62	SDSS	PAS	2	c	0	1
NGC5838	-6.16	2.90	-13.42	0.16	-3.83	3.24	-12.28	0.26	-1.42	HO	AGN	2	c	1	1
NGC5839	2.75	1.29	-	-	-0.13	1.55	<-14.49	1.41	<-3.62	LOI	PAS	3	-	-	1
NGC5845	1.92	1.27	-	-	1.15	1.27	-	-	-	LOI	PAS	3	-	0	1
NGC5846	-5.78	1.35	-13.81	0.18	-4.33	2.22	-12.19	0.33	-1.24	NED	AGN	2	d	1	1
NGC5854	7.37	1.29	-	-	-1.60	1.40	<-13.13	0.47	<-2.11	LOI	RET	3	-	0	1
NGC5864	-0.03	1.37	<-16.21	1.95	-0.70	1.54	<-13.50	0.77	<-2.39	LOI	PAS	3	-	-	1
NGC5869	-1.91	2.98	-14.11	0.40	0.18	3.52	-	-	-	LOI	PAS	3	-	-	1
PGC054452	1.36	1.50	-	-	3.00	1.36	-	-	-	SDSS	PAS	3	-	-	1
NGC6010	0.86	1.38	-	-	-1.24	1.39	<-13.37	0.54	<-2.21	LOI	PAS	3	-	0	1
NGC6014	-105.10	2.05	-13.04	0.01	-13.99	2.07	-12.56	0.12	-1.27	LOI	HII	1	d	1	1
NGC6017	0.19	2.91	-	-	3.15	2.93	-	-	-	LOI	RET	3	-	-	1
PGC056772	-57.28	1.83	-13.43	0.02	-13.75	1.76	-13.03	0.10	-1.65	SDSS	HII	1	c	-	1

Table 7. H α photometric parameters of the 147 observed galaxies

Galaxy	EW_{3^*} Å	\pm Å	$LogF_{3^*}$ erg cm ⁻² s ⁻¹	\pm erg cm ⁻² s ⁻¹	EW_{Tot} Å	\pm Å	$LogF_{Tot}$ erg cm ⁻² s ⁻¹	\pm erg cm ⁻² s ⁻¹	log SFR $M_{\odot}yr^{-1}$
NGC2480	-180.5	8.90	-13.38	0.01	-28.15	4.74	-12.81	0.06	-1.55
NGC2779	-4.14	3.22	-14.77	0.25	-13.95	3.14	-13.2	0.09	-2.01
NGC5636	-42.72	3.87	-13.82	0.03	-2.41	3.82	-13.48	0.41	-1.72
J125830	-215.4	8.89	-14.45	0.03	-84.28	4.55	-13.93	0.06	-1.83
J125838	-41.59	4.07	-14.73	0.08	-32.7	3.40	-13.99	0.08	-2.30
J125853	-27.99	4.13	-14.88	0.15	-22.1	3.77	-14.53	0.17	-1.20
J125916	-42.96	4.02	-13.98	0.07	-39.71	3.87	-13.38	0.07	-2.72
J130045	-0.59	8.71	-17.38	1.63	-35.39	6.18	-14.9	0.17	-1.68
J130254	-212.1	8.20	-14.36	0.03	-135.8	5.35	-13.97	0.04	-2.43
J162054	-55.9	5.16	-14.3	0.07	-74.44	4.85	-13.34	0.05	-1.03
J162431	-240.3	8.73	-13.87	0.03	-135.5	6.14	-13.31	0.04	-0.99
J162447	-10.41	5.54	-14.91	0.31	-11.98	4.95	-13.44	0.26	-1.10
J162549	-131.3	5.72	-13.38	0.03	-98.52	4.99	-12.53	0.04	-0.22
J162715	-41.02	4.60	-14.41	0.08	-17.81	3.80	-13.83	0.15	-1.65
J162820	-24.05	4.95	-14.55	0.15	-9.73	4.67	-13.91	0.29	-1.60
J162828	-9.44	4.21	-15.17	0.35	-11.55	3.9	-13.88	0.28	-1.58
J162915	-49.69	5.34	-14.41	0.11	-45.28	4.86	-13.47	0.11	-1.14
J162916	-26.51	4.54	-14.96	0.17	-47.82	4.18	-13.55	0.09	-1.26
J163037	-101.0	4.72	-14.07	0.05	-61.32	3.96	-13.24	0.07	-1.00
J163158	-26.49	5.04	-14.91	0.14	-49.65	4.42	-13.71	0.07	-1.43

Table 8. H α photometric parameters of the 20 filler galaxies





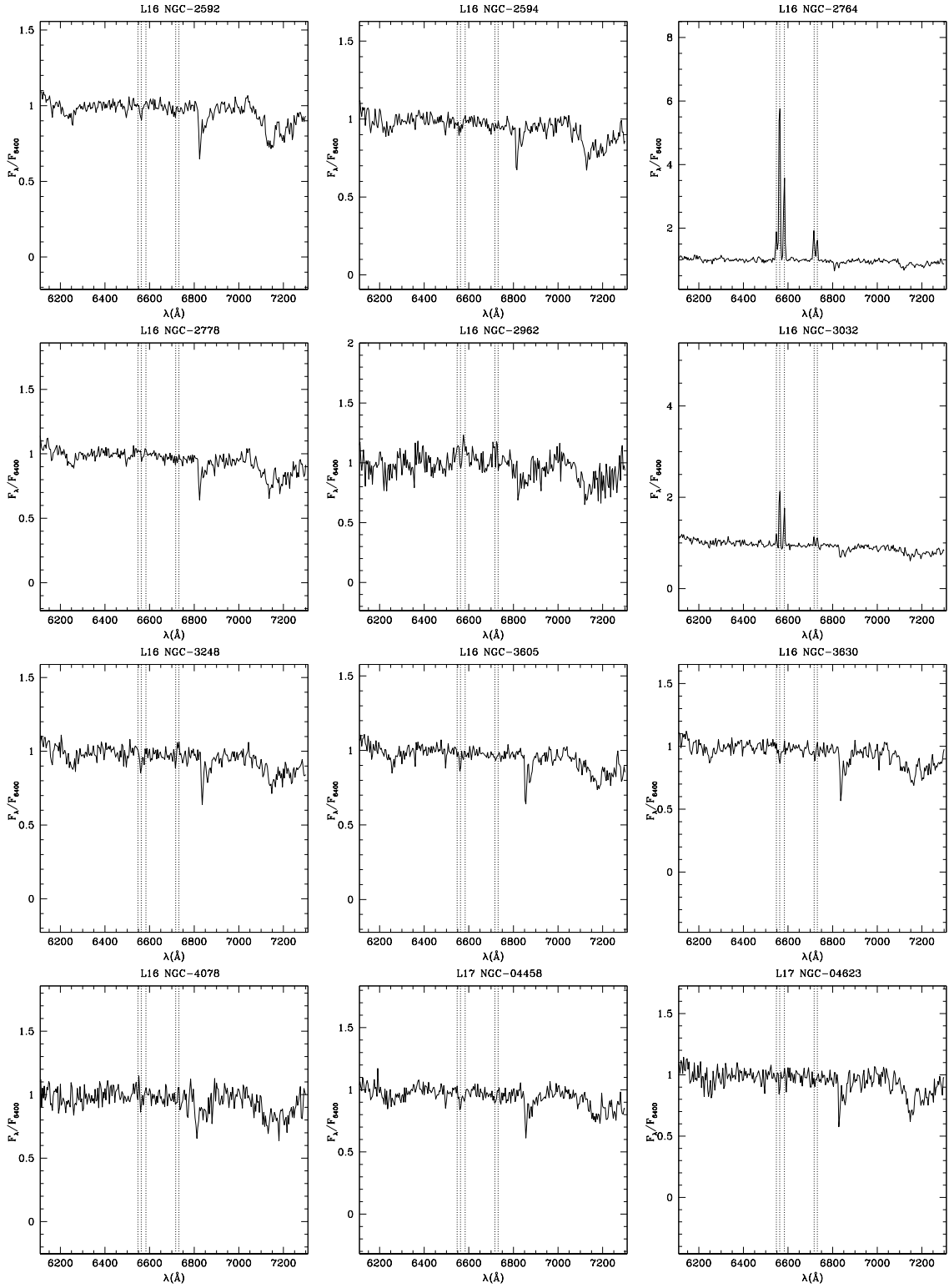


Fig. 12. Spectra taken at Loiano with the red grism covering from approximately 6200 to 7200 Å. The spectra have been Doppler shifted to λ_0 and normalized to the flux in the interval 6400–6500 Å. The vertical broken lines mark the rest-frame position of [NII] $\lambda 6549$; $H\alpha$ $\lambda 6563$; [NII] $\lambda 6584$; [SII] $\lambda 6717$, and [SII] $\lambda 6731$.

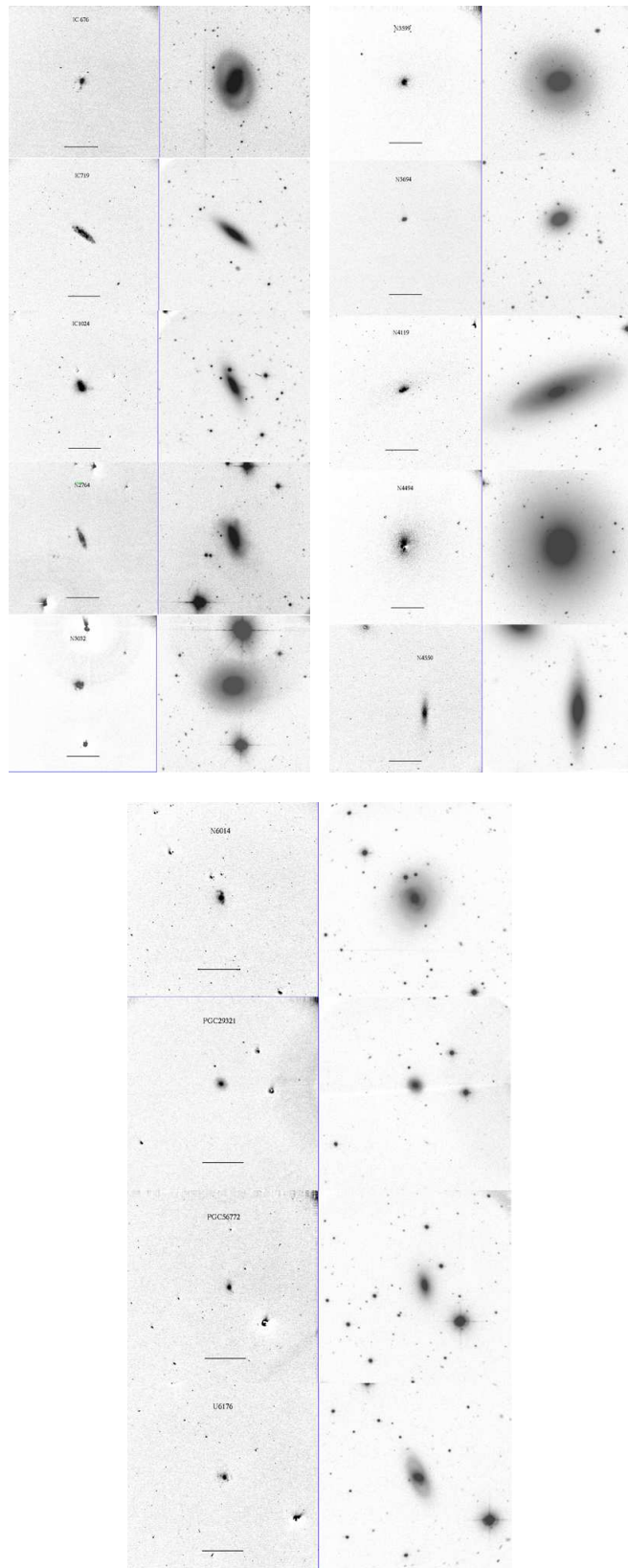


Fig. 13. NET (left) and OFF (right) images of 14 galaxies with strong $H\alpha$ detections (in the present observation campaign). North is up and east is to the left. A 1 arcmin bar is given in all images.

